
MULTI-SCALE KINETICS MODELING FOR CELL CULTURE PROCESS WITH METABOLIC STATE TRANSITION

Keqi Wang¹, Sarah W. Harcum^{*,2}, and Wei Xie^{†,1}

¹Department of Mechanical and Industrial Engineering, Northeastern University, Boston, MA 02115, USA

²Department of Bioengineering, Clemson University, Clemson, SC, USA

ABSTRACT

To advance the understanding of cellular metabolisms and control batch-to-batch variations in cell culture processes, a multi-scale mechanistic model with a bottom-up and top-down structure was developed to simulate the dynamics of cell culture process undergoing metabolic state transitions. This model integrates interactions at the molecular, cellular, and macro-kinetic levels, accounting for inherent variations in metabolic state transitions of individual cells. By incorporating both online (e.g., oxygen uptake, pH) and offline measurements (e.g., viable cell density, metabolite concentrations), the proposed mechanistic model enables accurate long-term prediction of cell culture trajectories and provides reliable prediction intervals quantifying batch-to-batch variations. This work can guide optimal design of experiments and robust process control to improve yield and production stability. Additionally, the proposed multi-scale model with a modular design enables flexible *in silico* simulations and extrapolation across diverse conditions, providing a robust prediction framework for scalable and flexible biomanufacturing applications.

Keywords Stochastic molecular reaction network, cell metabolism, prediction risk quantification, metabolic flux dynamics and analysis, cell classification

1 Introduction

Over the past several decades, biopharmaceuticals have gained prominence due to significant impact on public health, particularly highlighted by the production of COVID-19 vaccines and therapeutics. The market value of biopharmaceuticals reached \$343 billion in 2021, with 67% (107 out of 159) of approved recombinant products produced using mammalian cell systems. Chinese hamster ovary (CHO) cells are used predominantly, accounting for 89% of mammalian cell-derived products [56]. CHO cells are preferred over other eukaryotic hosts like yeast, mouse myeloma, HEK 293, and insect cell lines due to its ability to produce recombinant proteins that closely mimic human-like glycoforms, an essential quality for many treatments. This capability, combined with genetic adaptability and resilience under harsh conditions typical in late-stage fed-batch cultures, underscores its critical role in biopharmaceutical manufacturing [22]. However, like all mammalian cell cultures, CHO cells remain sensitive to variations in culture conditions, which can significantly impact yield, increase the heterogeneity of cell populations, and consequently affect the critical quality attributes (CQAs) of protein products [12]. This inherent heterogeneity also contributes to batch-to-batch variations, as not all cells within a bioreactor undergo metabolic state shifts simultaneously, even when exposed to the identical microenvironmental conditions.

To better understand and accurately replicate cellular behavior under various conditions, metabolic flux analysis (MFA) [38, 39, 2, 3, 45, 48, 58, 43, 11, 30] and kinetic modeling [29, 39, 14, 15, 16] have demonstrated strong potential for analyzing metabolic flux rates and other critical cellular activities. By providing a comprehensive framework for simulating cellular dynamics, these models enhance the understanding of underlying metabolic mechanisms and enable the strategic optimization of culture conditions. MFA quantifies metabolic flux rates, such as substrate uptake and metabolite secretion rates, under stoichiometric constraints. By assuming a pseudo-steady state for intracellular metabolites—where the sum of all fluxes producing a metabolite equals the sum of all fluxes consuming it—MFA

*Corresponding author: harcum@clemson.edu

†Corresponding author: w.xie@northeastern.edu

offers insights into the metabolic activities of different cell lines across various conditions. This analysis reveals how intracellular metabolites fluctuate during cell proliferation and respond to environmental changes, as detailed in studies by Niklas et al. (2012) [38] and others. Stable isotope techniques, such as ^{13}C labeling, when integrated with metabolic flux analysis, provide deeper insights into intracellular states and metabolic pathways, enabling precise estimation of metabolic reaction rates. Several modeling tools have been developed for situations involving isotopic and/or metabolic non-steady states [30, 2, 3].

To complement this, kinetic models typically using Monod and Michaelis–Menten kinetics delve into metabolic regulation mechanisms. Specifically tailored for CHO cell cultures, these models encompass key metabolic pathways like glycolysis, the pentose phosphate pathway (PPP), the tricarboxylic acid (TCA) cycle, and the respiratory chain. These models also consider the impact of energy shuttles (ATP/ADP) and cofactors (NADH, NAD^+ , NADPH, NADP^+), which are crucial for predicting cell responses to hypoxic perturbations. Notable studies, such as Ghorbaniaghdam et al. [14, 15, 16] and Nolan et al. (2011) [39], demonstrated how these models characterize cell flux rate responses to environmental perturbations and calculate extracellular metabolite consumption/production rates. For a more comprehensive discussion of metabolic flux analysis and kinetic modeling, refer to Antoniewicz (2015) [2] and Kyriakopoulos et al. (2018) [29].

Despite these advancements, metabolite heterogeneity within cell populations and inherent stochasticity of cell culture processes remain poorly understood, which are often not adequately considered during mechanistic model development [28, 52]. This gap results in several limitations: (a) a lack of reliable predictions and prediction uncertainty quantification accounting for batch-to-batch variations; (b) limited understanding of fundamental cell culture mechanisms and metabolic shifts, such as cellular responses to environmental changes and culture duration; (c) insufficient capability to integrate heterogeneous online and offline critical process parameters (CPPs) and critical quality attributes (CQAs) measurements and assay data; and (d) suboptimal control strategies for end-to-end cell culture processes.

To decode complex cellular metabolisms and facilitate well-controlled cultivation process dynamics, a multi-scale mechanistic model with a bottom-up and top-down hierarchical structure was developed, leveraging insights from individual cell metabolism studies to enhance the prediction and optimization of CHO cell culture processes. First, the model captures dynamic interactions between cultivation environmental changes, individual cell behaviors, and culture aging by focusing on regulatory mechanisms of cellular metabolic networks and accounting for cell heterogeneity induced by metabolic state transitions. This mechanistic model provides reliable predictions and quantifies the uncertainty of cell growth, metabolite profiles, and metabolic state shifts. Second, the model characterizes causal interdependencies from molecular to cellular to macro-kinetic levels and integrates both online and offline heterogeneous data, including (a) daily measurements of viable cell density (VCD), concentrations of critical metabolites (such as glucose, lactate, glutamine, glutamate, and ammonia) and amino acid, and the production titer of target monoclonal antibodies (mAbs); and (b) real-time measurements of volume, pH, stir speed, temperature, and gas flow rates. This comprehensive data integration enhances the understanding of central metabolic mechanisms and cell response to changes in feeding strategies, oxygen control, and environmental changes. Third, the mechanistic model has a modular design facilitating *in silico* simulations of different cell culture processes and supporting scalable and adaptable biomanufacturing.

Therefore, the proposed multi-scale mechanistic model and predictive analysis framework supports the integration of heterogeneous data, benefits the fundamental understanding of individual cell metabolism, and provides reliable extrapolated and long-term predictions with prediction interval (PI) quantifying batch-to-batch variations, thereby offering a robust framework for strategically optimizing cell culture processes under different environmental conditions.

2 Data Description and Analysis

2.1 Description of Online and Offline Experimental Data

A recombinant CHO-K1 cell line, clone A11, expressing the anti-HIV antibody VRC01 (IgG1), was used (donated by NIH). The experiments were conducted with a 12-way ambr250 HT bioreactor system (Sartorius Stedim, Göttingen, Germany). The bioreactors were inoculated at a target seeding density of 0.4×10^6 cells/mL and a working volume of about 210 mL in ActiPro media (Cytiva), supplemented with 6 mM of glutamine. Two culture scenarios, referred to as Case A and Case B, were each conducted in triplicate. Both cases used a pyramid feeding strategy up to day 11: 3%/0.3% (v/v) from Days 3 to 5, 4%/0.4% (v/v) on Days 6 to 7, 5%/0.5% (v/v) on Days 8 to 9, and then reverting to 4%/0.4% (v/v) on Days 10 to 11, with Cell Boost 7a/b (Cytiva). For Case A, the feeding was reduced to 3%/0.3% (v/v) starting on Day 12. Case B used a 4%/0.4% (v/v) feeding on Day 12, then 3%/0.3% (v/v) daily onward.

Dissolved oxygen (DO) levels were controlled to 50% air saturation using a proportional-integral-derivative (PID) control system, with parameter settings derived from Harcum et al. (2022) [21]. Cultures were stopped when cell

viability fell below 70%. The experimental settings and analytical methods employed are described in Harcum et al. (2022) and Chitwood et al. (2023)[21, 6].

Off-line Measurements: Daily samples were taken prior to feeding the additions to assess various critical process parameters (CPPs). These parameters included VCD and cell viability, which were measured using the trypan blue exclusion method with a Vi-Cell XR cell viability analyzer (Beckman Coulter, Brea, CA). Additionally, extracellular glucose, lactate, glutamine, glutamate, ammonia, and titer concentrations were analyzed using a Cedex Bioanalyzer (Roche Diagnostics, Mannheim, Germany). Amino acid concentrations were obtained using a capillary electrophoresis with high pressure mass spectrometry (CE-HPMS) analyzer (REBEL, 908 Devices, Boston, MA).

On-line Measurements: The ambr250 system monitored an extensive array of parameters in real time. These included vessel volume, feed and sampling volumes, pH, stir speed, temperature, DO levels, as well as the inlet and off-gas concentrations and flow rates for air, oxygen (O₂), and carbon dioxide (CO₂).

2.2 Cell-specific Oxygen Uptake Rate

The cell-specific oxygen uptake rate, denoted as qO_2 , is a vital parameter for characterizing CHO cell cultures, as it reflects the metabolic activity through pathways like glycolysis and the TCA cycle [4]. Studying qO_2 provides insights into cellular metabolism and helps optimize the CPPs by enabling precise control of oxygen levels in the culture environment. It is calculated by dividing the oxygen uptake rate (OUR) by the VCD, as shown in the equation below:

$$qO_2 = \frac{OUR}{VCD}. \quad (1)$$

The estimation of OUR is based on the oxygen transfer rate (OTR), which is influenced by several bioreactor parameters such as stir speed, gas flow rates, and oxygen concentrations. The mathematical derivation to estimate the OUR from OTR is described by Equation (2)

$$\frac{dC_L}{dt} = OTR - OUR, \quad (2)$$

where C_L represents liquid oxygen concentration (mg/L). For a short time duration, the change $\frac{dC_L}{dt}$ can be assumed to be small in comparison to both OUR and OTR. Consequently, OUR can be considered equal to OTR [53]. The final equation used in this study for calculating OTR is:

$$OTR = K^*(n^3)^a \left(\frac{M_f}{V}\right)^b \left(\frac{C_{cal}^*y_0}{y_{0,cal}} - C_{cal}^* \frac{DO}{100}\right),$$

where OTR (mg/L·h) is the oxygen transfer rate, representing the rate of oxygen transfer into the liquid medium per unit volume per hour, K^* (unitless) is an empirical constant specific to the bioreactor configuration and operating conditions, and n (rps) denotes the stir speed. The exponents a and b (unitless) are empirical constants specific to the bioreactor configuration and operating conditions. M_f (mL/min) is the total gas mass flow rate into the bioreactor, and V (L) is the liquid volume in the bioreactor. C_{cal}^* (mg/L) is the liquid oxygen saturation constant at calibration. y_0 (mol%) is the inlet oxygen concentration, and $y_{0,cal}$ (mol%) is the calibrated inlet oxygen concentration used as the reference during calibration. Lastly, DO (%) is the dissolved oxygen level, expressed as a percentage of air saturation. For a detailed derivation and description of the OTR calculation, refer to Appendix A.

2.3 Biomass and Target Protein

Széliová et al. (2020) reported the dry weight of the CHO-K1 cell line as 252.3 pg/cell, along with a detailed analysis of its biomass composition [50]. The amino acid sequence for the VRC01 antibody was derived by translating the DNA sequence from Synoground et al. (2021) [49] and shown in Appendix B.

3 Multi-Scale Mechanistic Modeling for Cell Culture with Metabolic State Shift

During cell culture processes, as the environmental conditions change and the culture time increases, cells often experience metabolic phase shifts that prompt cells to adjust regulatory metabolic networks and result in altered patterns of metabolic flux rates. Importantly, due to inherent cell-to-cell variations, not all cells within the bioreactor experience these shifts in metabolic state at the same time, even when exposed to identical microenvironments. For CHO cells,

it is common to observe lactate production initially, then a switch to lactate consumption [60, 51, 31, 35]. However, this metabolic shift does not occur uniformly for all cells in a culture nor for all cultures [36]. Therefore, this section presents the proposed multi-scale mechanistic model with bottom-up and top-down structure designed to capture the causal interdependency from individual cell behavior to macroscopic kinetics of heterogeneous cell population throughout the culture process, as well as the dynamic interactions among system-level environmental factors (such as environmental changes caused by feeding decisions). This mechanistic model characterizes the changes of cellular regulatory metabolic mechanisms and accounts for cell-to-cell variations in metabolic state transitions. Additionally, the model facilitates the integration of heterogeneous online and offline measurements to provide reliable long-term predictions with prediction interval (PI) quantifying batch-to-batch variations. Figure 1 provides an illustration of the proposed multi-scale mechanistic model for the CHO cell culture composed of heterogeneous cell populations in different metabolic states.

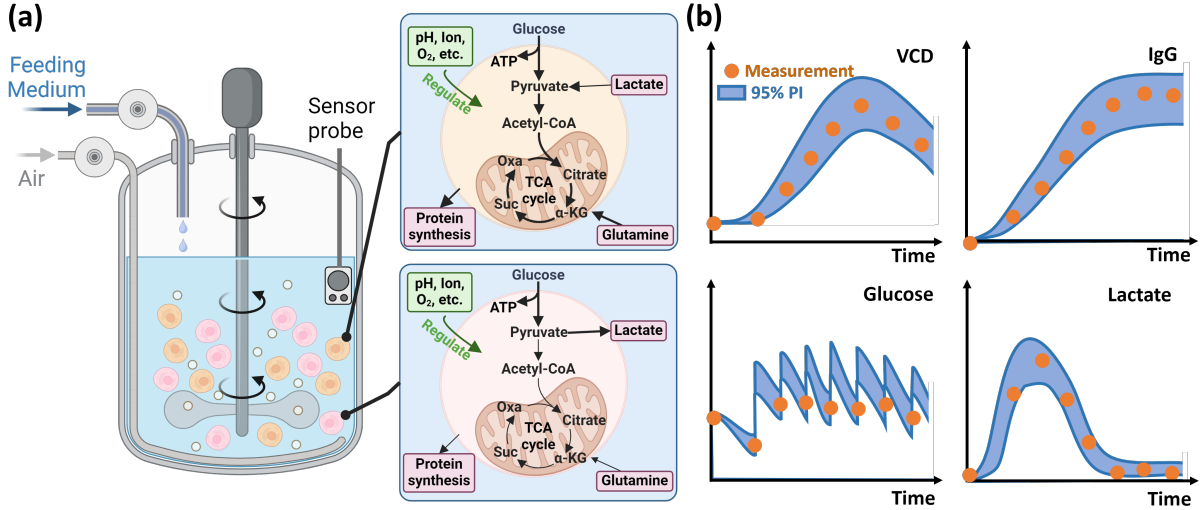


Figure 1: Schematic illustration of the multi-scale mechanistic modeling for cell culture process. (a) Within the bioreactor, the metabolic flux patterns are expected to shift significantly throughout the culture in response to environmental changes and culture ages; (b) Results of risk-based cell culture trajectory predictions for viable cell density (VCD), IgG, glucose, and lactate based on the proposed model, which takes into account the stochastic nature of the bioprocess. Orange dots indicate actual measurements, while the blue area represents the 95% prediction interval (PI).

3.1 Model Development on Metabolic Phase Shift

Drawing on the insights from Johnston et al. (2007) and considering the periodic nature of the cell cycle, the model assumes that state transitions within the process occur exclusively at discrete time points [27]. Specifically, the total duration of cell culture, denoted as T , is partitioned into H time intervals of varying lengths, Δt_h , where $\Delta t_h = t_{h+1} - t_h$ and the intervals are indexed by h with $h = 0, 1, \dots, H - 1$. The state transition of the cell culture from time t_h to t_{h+1} is denoted by $p(\mathbf{s}_{t_{h+1}} | \mathbf{s}_{t_h}, \mathbf{a}_{t_h}; \boldsymbol{\theta})$, where \mathbf{s}_{t_h} represents the culture state, including extracellular metabolite concentrations \mathbf{u}_{t_h} and cell population \mathbf{X}_{t_h} . In this study, the action \mathbf{a}_{t_h} of interest focuses on feeding strategies. Here, $\boldsymbol{\theta}$ encompasses the collection of model parameters that characterizes both the culture process dynamics and variations. At any given time t_h , the appropriate action \mathbf{a}_{t_h} is taken according to the state \mathbf{s}_{t_h} , following a specific policy function, denoted as $\pi(\mathbf{a}_{t_h} | \mathbf{s}_{t_h})$; for example, the feeding strategies employed in this study are predetermined and detailed in Section 2.1.

The effects of the feeding strategies, \mathbf{a}_{t_h} , on culture state \mathbf{s}_{t_h} are considered as given and immediate impacts, modeled as the post-decision state, i.e., the post-feeding concentration adjustments $p(\mathbf{s}_{t_h^+} | \mathbf{s}_{t_h}, \mathbf{a}_{t_h})$, where $\mathbf{s}_{t_h^+}$ represents the culture state immediately after feeding and t_h^+ denotes a moment infinitesimally close to, but just after the action \mathbf{a}_{t_h} occurring at time t_h . Consequently, the state transition model of cell culture process can reflect the feeding impacts:

$$p(\mathbf{s}_{t_{h+1}} | \mathbf{s}_{t_h}, \mathbf{a}_{t_h}; \boldsymbol{\theta}) = \int p(\mathbf{s}_{t_{h+1}} | \mathbf{s}_{t_h^+}; \boldsymbol{\theta}) p(\mathbf{s}_{t_h^+} | \mathbf{s}_{t_h}, \mathbf{a}_{t_h}; \boldsymbol{\theta}) d\mathbf{s}_{t_h^+} = p(\mathbf{s}_{t_{h+1}} | \mathbf{s}_{t_h^+}; \boldsymbol{\theta}),$$

where the transition from \mathbf{s}_{t_h} to post-decision state $\mathbf{s}_{t_h^+}$ is deterministic and known, i.e., $\mathbf{s}_{t_h^+} = f(\mathbf{s}_{t_h}, \mathbf{a}_{t_h}; \boldsymbol{\theta})$.

Therefore, given the distribution of the initial state $p(\mathbf{s}_{i_0})$, actions $\{\mathbf{a}_{i_h}\}_{h=0}^{H-1}$, and model parameters $\boldsymbol{\theta}$, the joint distribution of the entire process trajectory $\boldsymbol{\tau} = (\mathbf{s}_{i_0}, \mathbf{s}_{i_0^+}, \mathbf{s}_{i_1}, \mathbf{s}_{i_1^+}, \dots, \mathbf{s}_{i_{H-1}}, \mathbf{s}_{i_{H-1}^+}, \mathbf{s}_{i_H})$ can be modeled as:

$$p(\boldsymbol{\tau}) = p(\mathbf{s}_{i_0}) \prod_{h=0}^{H-1} p(\mathbf{s}_{i_{h+1}} | \mathbf{s}_{i_h^+}; \boldsymbol{\theta}).$$

The state transition $p(\mathbf{s}_{i_{h+1}} | \mathbf{s}_{i_h^+}; \boldsymbol{\theta})$ is modeled using a multi-scale model with modular design, which incorporates three critical modules spanning from cellular- to macro-kinetics: (1) a stochastic mechanistic model for single-cell metabolic reaction network; (2) single-cell metabolic phase shift probabilistic model; and (3) macro-kinetics of a mixture heterogeneous cell population including cells in different metabolic phases. This accounts for the primary factors affecting process dynamics and variability in cell culture that are driven by cellular metabolisms [40].

Basically, the single-cell metabolic stochastic reaction model evaluates the impact of the environment on the intracellular flux rates that leads to subsequent changes in the consumption of extracellular substrates and the excretion of products/waste by individual cells. Since each individual cell may transition between different phases, a metabolic phase shift probabilistic model is proposed to capture this transition process. Then, the macro-kinetics model of a mixed cell population characterizes the dynamics of cell culture process. Thus, the proposed multi-scale mechanistic model integrates variable growth or decline rates of cells located in different metabolic phases, providing a detailed simulation of how diverse cellular states impact the overall macro-kinetics of the population over time.

(1) Stochastic Mechanistic Model for Single-cell Metabolic Reaction Network

The extracellular metabolite concentrations at time t are denoted by a vector with dimension m , i.e., $\mathbf{u}_t = (u_{1,t}, u_{2,t}, \dots, u_{m,t})^\top$. At any time t , let z_t represent the metabolic phase for single cell. In this study, three distinct phases are recognized: growth ($z_t = 0$), stationary ($z_t = 1$), and decline ($z_t = 2$). Cells exhibit markedly different behaviors across these phases. To model the dynamic evolution of cell response to environmental change during the cell culture process, at any time t , the specific reaction flux rates of cells in the z -th phase is represented by a vector,

$$\mathbf{v}^z[\mathbf{u}_t] = (v_1^z[\mathbf{u}_t], v_2^z[\mathbf{u}_t], \dots, v_n^z[\mathbf{u}_t])^\top.$$

To capture the cell response to environmental perturbation, a Michaelis–Menten (M-M) formalism was used to characterize the relationship of metabolic flux rates dependency on the concentrations of associated substrates and inhibitors [29]. This allows the model to leverage the existing biological knowledge and facilitated the learning of regulation mechanisms from the experimental data.

Specifically, at any time t , the g -th pathway flux rate of a single cell in the z -th phase is modeled as,

$$v_g^z[\mathbf{u}_t] = v_{max,g,f}^z \prod_{k \in \Omega_K^{g,f}} \frac{u_{k,t}}{u_{k,t} + K_{m,k}^z} - v_{max,g,r}^z \prod_{k \in \Omega_K^{g,r}} \frac{u_{k,t}}{u_{k,t} + K_{m,k}^z},$$

for $g = 1, 2, \dots, n$ and $z = 0, 1, 2$, where n denotes the dimension of molecular reactions of interest, $v_{max,g,f}^z$ and $v_{max,g,r}^z$ represent phase-specific maximal flux rates from substrates to products (forward) and vice versa (backward). The sets $\Omega_K^{g,f}$ and $\Omega_K^{g,r}$ represent the collection of substrates influencing the forward and backward flux rates. The parameters $K_{m,k}^z$ represent the phase-specific M-M half-saturation constant. Various regulatory mechanisms, including allosteric regulation, competitive inhibition, and feedback inhibition, have been incorporated into the proposed metabolic flux kinetic model, as detailed in Section 4.1. These mechanisms play crucial roles in modulating enzyme activities and metabolic pathways, ensuring an accurate representation of the dynamic behavior of cell metabolic network.

Let \mathbf{N} denote an $m \times n$ stoichiometry matrix characterizing the structure of the metabolic reaction network. The (i, j) -th element of \mathbf{N} , denoted as $\mathbf{N}(i, j)$, represents the number of molecules of the i -th species that are either consumed (indicated by a negative value) or produced (indicated by a positive value) in each random occurrence of the j -th reaction. During the time interval $[t_h, t_{h+1})$, the exchange rate \mathbf{r}_t for m extracellular metabolites, representing nutrient uptake and metabolite secretion by a single cell, is described by the following stochastic differential equations (SDEs) that characterizes the metabolic flux rate variations of cells in the z -th metabolic phase:

$$\mathbf{r}_t = \mathbf{N}\mathbf{v}^z[\mathbf{u}_t]dt + \{\mathbf{N}\boldsymbol{\sigma}^z[\mathbf{u}_t]\mathbf{N}^\top\}^{\frac{1}{2}}d\mathbf{W}_t, \quad \text{for } t \in [t_h, t_{h+1}), z \in \{0, 1, 2\}, \text{ and } h \in \{0, 1, \dots, H-1\}, \quad (3)$$

where $\mathbf{N}\mathbf{v}^z[\mathbf{u}_t]dt$ represents the deterministic component or the population mean, capturing the cell's systemic metabolic activities. Meanwhile, the second term $\{\mathbf{N}\boldsymbol{\sigma}^z[\mathbf{u}_t]\mathbf{N}^\top\}^{\frac{1}{2}}d\mathbf{W}_t$ constitutes the stochastic component, which incorporates randomness via an m -dimensional standard Wiener process (Brownian motion), $d\mathbf{W}_t$, characterizing the variation of molecule-to-molecule interactions. This term incorporates variability and randomness due to factors like

molecular collisions and fluctuations in enzyme activity, providing a more realistic representation of cellular dynamics and cell-to-cell variations.

Given the current state \mathbf{u}_t , the reaction rates of n different molecular reactions are assumed to be conditional independence of each other. Following Gillespie (1977) [17] and Gillespie (2000) [18], under the Poisson assumption, the relationship $\boldsymbol{\sigma}^z[\mathbf{u}_t] = \text{diag}(\mathbf{v}^z[\mathbf{u}_t])$ holds. In addition, to enhance prediction performance and account for more complex situations (such as some latent factors that further lead to different classes of cells), a proportional term can be introduced as $\boldsymbol{\sigma}^z[\mathbf{u}_t] = \boldsymbol{\epsilon} \text{diag}(\mathbf{v}^z[\mathbf{u}_t])$, where $\boldsymbol{\epsilon}$ is a diagonal matrix with diagonal elements $\{\epsilon_1, \epsilon_2, \dots, \epsilon_n\}$ representing the reaction-specific coefficients of variation and it can be further extended to be metabolic phase dependent if needed. The values of $\boldsymbol{\epsilon}$ will be learned from the experimental data.

(2) Single-cell Metabolic Phase Shift Probabilistic Model

At any given discrete transition point t_h , the phase transition matrix \mathbf{P}_{t_h} is formulated to characterize the single-cell transition probabilities from the previous growth ($z_{t_h} = 0$), stationary ($z_{t_h} = 1$), or decline ($z_{t_h} = 2$) phases to next phase. Specifically, the (i, j) -th element within the matrix \mathbf{P}_{t_h} , denoting the probability of a metabolic phase transition of a single cell from phase i to phase j , is represented by a sigmoid function of environmental conditions and culture time, i.e.,

$$p^{ij}[t_h, \mathbf{u}_{t_h}, qO_{2,t_h}] = P(z_{t_{h+1}} = j | z_{t_h} = i, t_h, \mathbf{u}_{t_h}, qO_{2,t_h}) = \frac{1}{1 + \exp^{-(\beta_0^{ij} + \beta_1^{ij} \times t_h + \beta_2^{ij} \times qO_{2,t_h} + \sum_{k \in \Omega^{ij}} \beta_k^{ij} \times v_k^i[\mathbf{u}_{t_h}])}}, \quad (4)$$

for any metabolic phase $i, j \in \{0, 1, 2\}$ and time index $h = 0, 1, \dots, H-1$. This probability is estimated based on several key indicators: culture aging t_h , the oxygen uptake rate qO_{2,t_h} , and the production or consumption rate $v_k^i[\mathbf{u}_{t_h}]$ of essential metabolite k within the set Ω^{ij} . The set Ω^{ij} comprises metabolites that serve as critical indicator for metabolic phase transitions from phase i to j , with the rates $v_k^i[\mathbf{u}_{t_h}]$ influenced by the extracellular metabolite concentrations \mathbf{u}_{t_h} .

To control model complexity and avoid collinearity caused by the high correlations between indicators, the probabilistic phase shift model in Equation (4) is simplified as follows:

$$p^{ij}[t_h, qO_{2,t_h}] = P(z_{t_{h+1}} = j | z_{t_h} = i, t_h, qO_{2,t_h}) = \frac{1}{1 + \exp^{-(\beta_0^{ij} + \beta_1^{ij} \times t_h + \beta_2^{ij} \times qO_{2,t_h})}},$$

where only two online measurements, culture aging t_h and the oxygen uptake rate qO_{2,t_h} are used. These indicators effectively reflect metabolic activity and facilitate real-time monitoring. Despite this simplification, the prediction performance of the proposed multi-scale mechanistic model remains robust, as detailed in Section 4.2.

(3) Macro-Kinetics of a Mixture Cell Population

Next, a mechanistic model is constructed to characterize cell growth and the distribution dynamics of a mixed cell population, accounting for the varying growth rates of cells in different metabolic phases. In specific, at any time t , let $\mathbf{X}_t = (X_t^0, X_t^1, X_t^2)^\top$ denote the density distribution of cells located in each phase for $z = 0, 1, 2$ (i.e., growth, stationary, and decline phases). The model for the dynamic change in the cell population distribution during time interval $[t_h, t_{h+1})$, taking into account different growth rates of cells located in each phase z , is expressed as:

$$dX_t^z = \mu^z[\mathbf{u}_t] X_t^z dt + \{\sigma_\mu^z[\mathbf{u}_t]\}^{\frac{1}{2}} X_t^z dW_t, \text{ for } z \in \{0, 1, 2\}, t \in [t_h, t_{h+1}), \text{ and } h \in \{0, 1, \dots, H-1\}, \quad (5)$$

where dW_t as a Wiener process (Brownian motion) characterizes the cell growth variations. The deterministic term of cell growth $\mu^z[\mathbf{u}_t]$ is formulated using M-M kinetics to characterize the expected impact of extracellular metabolite concentrations, as detailed in Table A.1 in Appendix E. Under the Poisson assumption, the relationship $\sigma_\mu^z[\mathbf{u}_t] = \mu^z[\mathbf{u}_t]$ holds for $z \in \{0, 1, 2\}$.

Therefore, built on the single-cell metabolic phase transition matrix \mathbf{P}_{t_h} , the proportion of cells transiting between different phases at time t_h can be formulated as follows:

$$\mathbf{X}_{t_h}^\top = \mathbf{X}_{t_h^-}^\top \mathbf{P}_{t_h}, \text{ for } h \in \{0, 1, \dots, H-1\}, \quad (6)$$

where $\mathbf{X}_{t_h^-}$ denotes the cell population vector immediately before the transition at time t_h and t_h^- represents a moment infinitesimally close to, but just before, t_h .

Meanwhile, based on the single-cell metabolic stochastic model in Equation (3), during the time interval $[t_h, t_{h+1})$, the change in the extracellular metabolite concentrations due to the behavior of the mixed cell population is described by the following SDE:

$$d\mathbf{u}_t = \sum_{z \in \{0, 1, 2\}} X_t^z \mathbf{N} \mathbf{v}^z[\mathbf{u}_t] dt + \sum_{z \in \{0, 1, 2\}} \sum_{i=1}^{X_t^z} \{\mathbf{N} \boldsymbol{\sigma}^z[\mathbf{u}_t] \mathbf{N}^\top\}^{\frac{1}{2}} d\mathbf{W}_{t,i}, \text{ for } t \in [t_h, t_{h+1}) \text{ and } h \in \{0, 1, \dots, H-1\}, \quad (7)$$

where X_i^z for $z \in \{0, 1, 2\}$ denotes the VCD in the growth, stationary, and decline phases respectively. This model sums the impacts from a heterogeneous cell population distributed in different metabolic phases, capturing varied metabolic activities and highlighting the role of stochastic factors in complex cell culture processes.

3.2 Regulatory Metabolic Reaction Network for Single Cell

The metabolic reaction network for mammalian cell is illustrated in Figure 2 and includes central carbon metabolism [16, 15, 39, 57]. The stoichiometry of all relevant reactions for CHO cell cultures is provided in Table A.1 in Appendix F, encompassing glycolysis, the TCA cycle, anaplerosis, amino acid metabolism, and reactions associated with metabolite import and export. For simplification, the reactions related to branched-chain amino acids (BCAAs), were collapsed based on insights from several studies [46, 32, 10, 24, 37]. Hundal et al. (1989) [25] and Nolan et al. (2011) [39] reported that the K_m (M-M half-saturation constant) for most metabolite transporters is significantly higher than the extracellular concentration of the metabolites. This indicates that metabolite exchange is primarily regulated by intracellular enzymes rather than the corresponding extracellular metabolite transporters. Therefore, the reaction rates of cytosolic and mitochondrial intracellular enzyme-catalyzed processes, described by the M-M formalism-based regulation model, mainly depend on the extracellular metabolite concentrations. Reactions highlighted in red in Figure 2 are those with regulation model constructed using the M-M formalism as described in Equation (3). For the remaining reactions highlighted in black, the pseudo-steady state assumption is applied. The comprehensive reaction rate model is provided in Appendix Table A.2, while Table A.3 lists the full names and abbreviations of the metabolites.

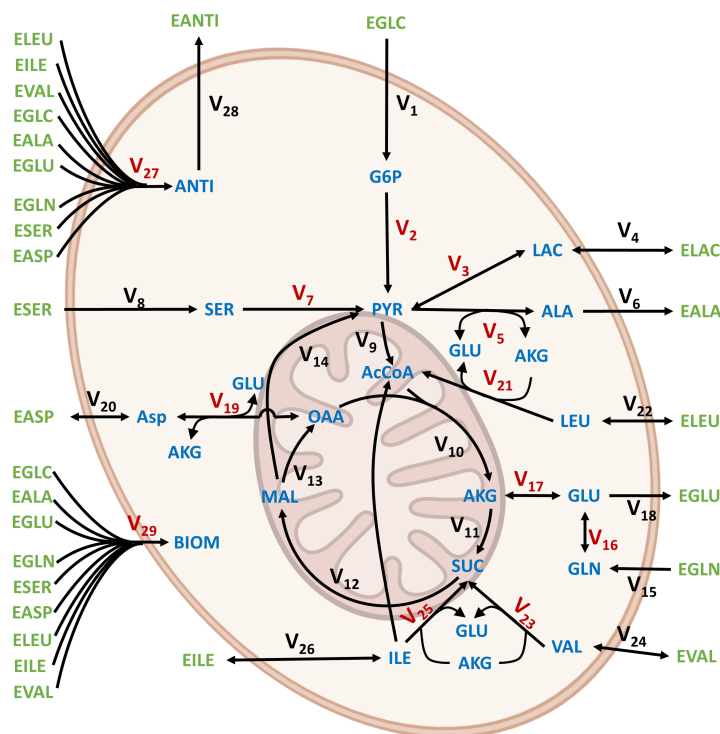


Figure 2: Schematic of the CHO Metabolic Reaction Network. Metabolites are shown in green and blue for extracellular and intracellular, respectively. The reactions in the mitochondria include the conversion of pyruvate to acetyl-CoA and the TCA cycle. For simplicity, cytosolic and mitochondrial pyruvate are shown as a single species. Reactions with flux rate modeling using M-M kinetics are shown in Red.

3.3 Model Inference and Goodness-of-fit Assessment

(1) Continuous Time Mechanistic Model Approximation

The Euler-Maruyama algorithm [47] was employed to approximate the dynamics of the proposed cell culture model, addressing the typically intractable nature of solutions to the associated SDEs. The cell population dynamics model,

incorporating both cell growth (Equation (5)) and metabolic phase transitions (Equation (6)), is formulated as:

$$\mathbf{X}_{t_{h+1}}^\top = (\mathbf{X}_{t_h} + \mathbf{M}_{t_h} \mathbf{X}_{t_h} \Delta t + \mathbf{S}_{t_h}^{\frac{1}{2}} \mathbf{X}_{t_h} \Delta \mathbf{W}_{t_h})^\top \mathbf{P}[\mathbf{s}_{t_h}], \text{ for } h \in \{0, 1, \dots, H-1\}, \quad (8)$$

where \mathbf{X}_{t_h} and $\mathbf{X}_{t_{h+1}}$ represent the cell population vectors at times t_h and t_{h+1} , respectively. The matrix \mathbf{M}_{t_h} is a diagonal matrix where each diagonal element $\mu_{t_h}^z$ represents the growth rate for cells in the corresponding phase $z = \{0, 1, 2\}$ at time t_h . It is structured as $\mathbf{M}_{t_h} = \text{diag}(\mu^0[\mathbf{u}_{t_h}], \mu^1[\mathbf{u}_{t_h}], \mu^2[\mathbf{u}_{t_h}])$, and $\mathbf{S}_{t_h} = \text{diag}(\sigma_\mu^0[\mathbf{u}_{t_h}], \sigma_\mu^1[\mathbf{u}_{t_h}], \sigma_\mu^2[\mathbf{u}_{t_h}])$ is a diagonal matrix of stochastic fluctuation intensities. The vector $\Delta \mathbf{W}_{t_h}$ contains Wiener process increments during the interval $[t_h, t_{h+1})$, each following a normal distribution with mean 0 and variance $\Delta t = t_{h+1} - t_h$, denoted as $\Delta W_{t_h}^z \sim \mathcal{N}(0, \Delta t)$ for each phase z . Therefore, this kinetic formulation (8) accounts for the dynamics induced by cell growth and metabolic phase transitions, accommodating for different growth rates of a mixture cell population distributed in phases $z = \{0, 1, 2\}$ before undergoing transitions as described by the matrix \mathbf{P}_{t_h} .

Further, the dynamics of the extracellular metabolites, as indicated by Equation (7), is formulated as follows:

$$\mathbf{u}_{t_{h+1}} = \mathbf{u}_{t_h} + \sum_{z \in \{0,1,2\}} X_t^z \mathbf{N} \mathbf{v}^z[\mathbf{u}_t] \Delta t + \sum_{z \in \{0,1,2\}} \sum_{i=1}^{X_t^z} \{\mathbf{N} \sigma^z[\mathbf{u}_t] \mathbf{N}^\top\}^{\frac{1}{2}} \Delta \mathbf{W}_{t_h,i}, \text{ for } h \in \{0, 1, \dots, H-1\}, \quad (9)$$

where \mathbf{u}_{t_h} and $\mathbf{u}_{t_{h+1}}$ represent the extracellular metabolite concentrations at time t_h and t_{h+1} , respectively. The vector $\Delta \mathbf{W}_{t_h}$ contains Wiener process increments, each following a normal distribution with mean 0 and variance Δt , denoted as $\Delta W_{t_h}^z \sim \mathcal{N}(0, \Delta t)$ for each metabolic phase z . In sum, the parameters $\boldsymbol{\theta} = \{\mathbf{v}_{max}, \mathbf{K}_m, \boldsymbol{\beta}\}$ specify the proposed multi-scale mechanistic model with modular design: (1) The set of parameters $\{\mathbf{v}_{max}, \mathbf{K}_m\}$ characterizes cell dynamics and variations in response to environmental changes; and (2) $\boldsymbol{\beta}$ represents the impact of critical factors (i.e., the culture aging t_h and the oxygen uptake rate qO_{2,t_h}) on metabolic phase transitions.

(2) Model Inference

The proposed multi-scale cell culture process model utilizes the Euler approximation providing a linear representation of system dynamics. Given the relatively long sampling interval (≈ 1 Day) for offline measurements, this method may introduce non-negligible approximation errors as intermediate state transitions are not fully captured. To address this limitation while retaining the simplicity of the linear approximation, the Expectation-Maximization (EM) algorithm is used to interpolate intermediate state transitions between measurement points. Additionally, this EM approach can effectively handle scenarios where measurements are missing at predetermined sampling points, ensuring accurate state estimations even with incomplete dataset. Refer to Algorithm 1 on the EM model inference and latent state prediction in Appendix C for details. As a result, the refined state estimates improve the model's overall predictive capability, supporting more effective optimization of end-to-end bioprocess conditions.

(3) Goodness-of-fit Assessment

To support the robust optimization of cell culture process, the model predictions of mean and prediction interval (PI) of state trajectory $\{\mathbf{s}_{t_h}\}_{h=0}^H$, accounting for batch-to-batch variations, are evaluated. First, at any current time t_h , given the historical state observations of the cell culture process denoted as $\mathbf{s}_{[t_0:t_h]}$, the Weighted Absolute Percentage Error (WAPE) metric was used to evaluate the accuracy of the model prediction on the mean $E[\mathbf{s}_{t_{h+\ell}} | \mathbf{s}_{[t_0:t_h]}]$ for ℓ -step ahead trajectory predictions. WAPE quantifies the relative error between the prediction $\widehat{E}[\mathbf{s}_{t_{h+\ell}} | \mathbf{s}_{[t_0:t_h]}]$ and single measure value on $\mathbf{s}_{t_{h+\ell}}$ while accounting for the scale of the observations, ensuring robustness to variations in data magnitude:

$$\text{WAPE} = \frac{\sum_{h=0}^{H-\ell} \left| \mathbf{s}_{t_{h+\ell}} - \widehat{E}[\mathbf{s}_{t_{h+\ell}} | \mathbf{s}_{[t_0:t_h]}] \right|}{\sum_{h=0}^{H-\ell} \mathbf{s}_{t_{h+\ell}}} \times 100\%. \quad (10)$$

Second, given the historical observations of cell culture process, $\mathbf{s}_{[t_0:t_h]}$, the conditional distribution of a future state at time $t_{h+\ell}$, denoted as $p(\mathbf{s}_{t_{h+\ell}} | \mathbf{s}_{[t_0:t_h]})$, can be utilized to construct prediction intervals quantifying prediction uncertainty, i.e., a $(1 - \alpha)100\%$ two-sided percentile PI for the future state $\mathbf{s}_{t_{h+\ell}}$ defined as:

$$\widehat{\text{PI}}(\mathbf{s}_{t_{h+\ell}}) = [q_{\alpha/2}(\mathbf{s}_{t_{h+\ell}}), q_{1-\alpha/2}(\mathbf{s}_{t_{h+\ell}})],$$

where $q_{\alpha/2}(\mathbf{s}_{t_{h+\ell}})$ and $q_{1-\alpha/2}(\mathbf{s}_{t_{h+\ell}})$ represent the lower and upper percentile quantiles, respectively, of the cumulative distribution function for $p(\mathbf{s}_{t_{h+\ell}} | \mathbf{s}_{[t_0:t_h]})$. These quantiles determine the bounds of the interval within which the actual value of $\mathbf{s}_{t_{h+\ell}}$ is expected to fall with $(1 - \alpha)100\%$ confidence, thereby accounting for batch-to-batch variations and encapsulating forecast uncertainty. It typically becomes more challenging to predict accurately as the interval between t_h and $t_{h+\ell}$ increases.

To evaluate the efficacy and reliability of the probabilistic forecasts generated by the proposed multi-scale mechanistic model, the coverage of the prediction intervals for ℓ -step ahead cell culture trajectory predictions is examined through the following metric on coverage, i.e.,

$$\text{Coverage}(\mathbf{s}_{t_{h+\ell}}) = \frac{1}{H - \ell + 1} \sum_{h=0}^{H-\ell} \mathbb{1} \left(\mathbf{s}_{t_{h+\ell}} \in \widehat{\text{PI}}(\mathbf{s}_{t_{h+\ell}}) \right), \quad (11)$$

where $\mathbb{1}(\cdot)$ is an indicator function that returns 1 if its argument is true, i.e., if the measurement $\mathbf{s}_{t_{h+\ell}}$ falls within the predicted interval $\widehat{\text{PI}}(\mathbf{s}_{t_{h+\ell}})$, and 0 otherwise. The coverage effectively quantifies the proportion of times the measurements fall within the prediction intervals over $H - \ell + 1$ forecasting instances, offering insights into the predictive accuracy and reliability of the modeling approach in capturing the dynamics and uncertainties of cell culture trajectories.

4 Results and Discussion

4.1 Culture Profile and Regulatory Mechanisms

(1) Cell growth and productivity

Based on the cell growth and metabolite profile dynamics shown in Figure 3, the majority of the cell population gradually transits from exponential growth phase (day 0 to day 7) to stationary phase (day 7 to day 9), and eventually enters decline phase (day 9 onwards). No significant differences in growth patterns were observed between Case A and Case B, as illustrated in Figure 3(a) ($p > 0.05$). When comparing the IgG synthesis rates between Case A and Case B, it is evident that Case A exhibits a significantly higher rate throughout the process, as shown in Figure 3(f) ($p \leq 0.05$). This difference can be attributed to the consistently higher levels of branched-chain amino acids (BCAAs), specifically leucine and isoleucine, observed in Case A, as shown in Figures 3(g) and (h). BCAAs not only act as substrates for protein synthesis but also play a dual role in enhancing protein synthesis while simultaneously inhibiting proteolysis [24, 37]. The dynamic profiles of the remaining metabolites of interest (i.e., ammonia, alanine, aspartate, and serine) were shown in the left column of Figure A.1 in Appendix D.

The specific oxygen uptake rate, qO_2 , for each day of the fed-batch culture was determined in accordance with Equation (1) and illustrated in Figure 4. The Savitsky-Golay (SG) filter is utilized to reduce signal noise. Throughout the duration of the cultures, CHO cells display a rising trend in oxygen demand, which can be primarily ascribed to the enhanced activity of the TCA cycle. This increase in oxygen demand reflects the cells' escalated use of aerobic respiration, driven by the TCA cycle's critical role in energy production through the oxidation of acetyl-CoA, leading to the generation of NADH and FADH₂. Compared to Case B, Case A exhibits significantly higher oxygen uptake rates from day 9 onwards ($p \leq 0.05$), generating the energy needed to sustain its higher IgG synthesis rate.

(2) Regulatory mechanisms

During the cell culture processes, CHO cells typically experience multiple metabolic phases. In the early exponential growth phase, cells primarily utilize glucose and amino acids, including glutamine, glutamate, serine, leucine, isoleucine, and valine, as essential carbon sources. Figure 3(d) illustrates that as external glutamine supplies decreasing towards the end of this phase, the cell population responds by upregulating enzymes such as glutamine synthetase (GS), which plays a pivotal role in the internal synthesis of glutamine from glutamate and ammonia. Further, the Cell Boost 7b supplies glutamate, thereby maintaining glutamate availability to meet the metabolic demands of the culture.

As the culture transitions into the late exponential phases, a notable shift occurs in lactate metabolism from primarily production to consumption. This metabolic shift is prompted by the depletion of glutamine, leading to a reduced influx of carbon into the TCA cycle via alpha-ketoglutarate, and consequently, diminished NADH production. To compensate this, cells begin to utilize lactate present in the culture as an alternative carbon source. These cells effectively reverse the substrate preference for lactate dehydrogenase (LDH), converting lactate back into pyruvate. This process reduces lactate levels and generates the NADH [39]. Additionally, glutamine levels increase due to the addition of glutamate. As the culture approaches harvest, the cells' metabolic state shifts back to a low-lactate production state, potentially due to diminished mitochondrial function resulting from the accumulation of ROS after a high-productivity phase [20].

In addition to the regulatory mechanisms that primarily focus on substrate impacts, several critical regulatory mechanisms were introduced into the metabolic flux kinetics model to enhance predictive accuracy and more effectively capture cellular responses to environmental changes. These regulatory dependencies are described below, highlighted using brackets $\underbrace{\dots\dots}$, along with the corresponding regulatory mechanism numbers, while the original nomenclature is outside the brackets.

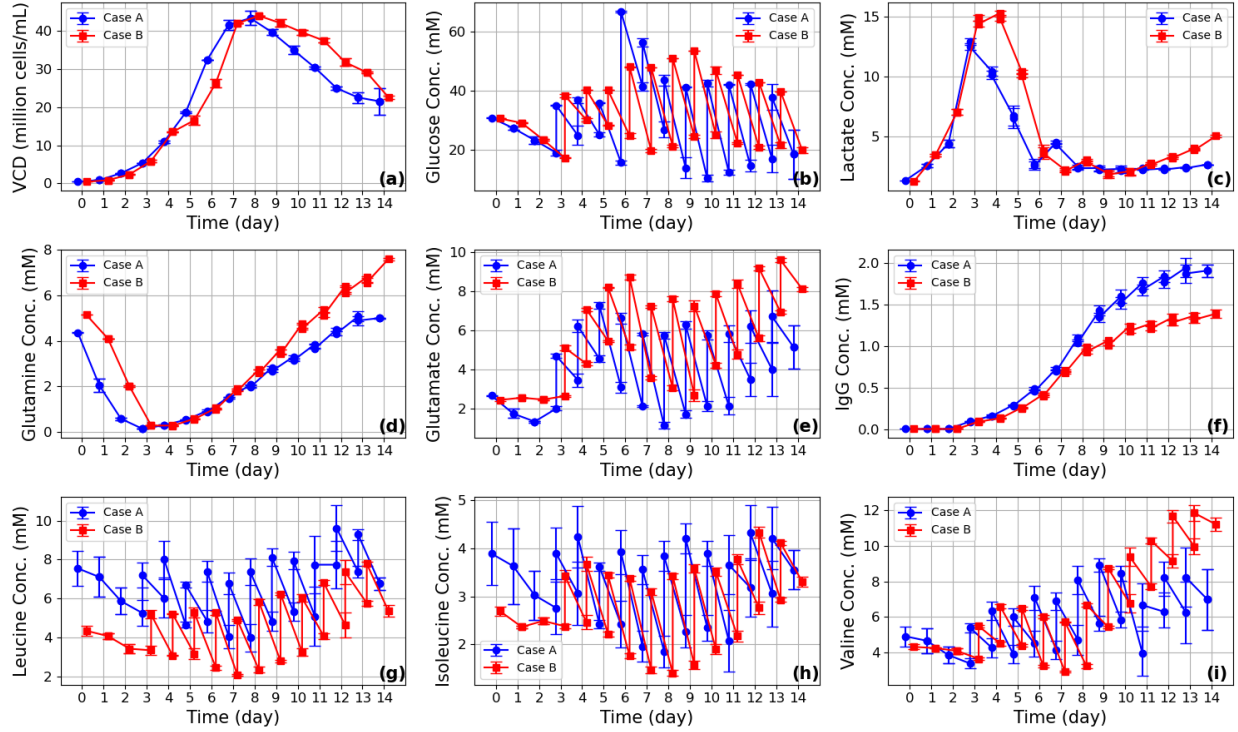


Figure 3: Growth and cell metabolite profile dynamics for CHO VRC01 cell cultures. Illustrated critical process parameters include: (a) VCD; (b) glucose; (c) lactate; (d) IgG (titer); (e) glutamine; (f) glutamate; (g) leucine; (h) isoleucine; and (i) valine. Case A cultures are depicted in blue, while Case B cultures are in red. The lines represent the mean values obtained from triplicate cultures, with error bars reflecting the standard deviations. To distinguish overlapping data points, a slight horizontal offset of 0.4 days has been applied between the data points for Case A and Case B.

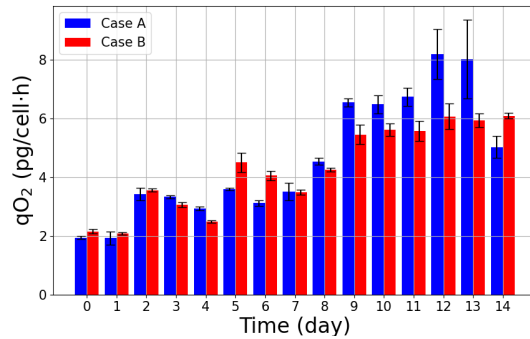


Figure 4: Cell specific oxygen uptake rates (qO_2) for the fed-batch CHO VRC01 cell cultures, i.e., Case A and B. The qO_2 values were determined from the OTR and VCD.

Lactate accumulation has previously been reported to reduce glycolytic activity by inhibiting hexokinase (HK) and phosphofructokinase (PFK) activity in mammalian cells, where lactate acts as a signaling molecule to down-regulate PFK activity [26, 35, 9]. The model for HK was updated to include this inhibitory effect of lactate on it:

$$v_2 = v_{max,2} \times \frac{EGLC}{K_{m,EGLC} + EGLC} \times \underbrace{\frac{K_{i,ELACtoHK}}{K_{i,ELACtoHK} + ELAC}}_{R1}$$

Since lactate inhibits glutaminase activity – the enzyme responsible for converting glutamine (GLN) to glutamate (GLU) [19, 23] – the forward (f) flux rate for the reaction, i.e., $\text{GLN} \leftrightarrow \text{GLU} + \text{NH}_4$, was updated,

$$v_{16} = v_{\max,16f} \times \frac{EGLN}{K_{m,EGLN} + EGLN} \times \underbrace{\frac{K_{i,ELACtoGLNS}}{K_{i,ELACtoGLNS} + ELAC}}_{\text{R2}} - v_{\max,16r} \times \frac{EGLU}{K_{m,EGLU} + EGLU} \times \frac{NH_4}{K_{m,NH_4} + NH_4}$$

During glutaminolysis, glutamine is converted into α -ketoglutarate, which can be used as an intermediate in the TCA cycle. As a result, glutamine can indirectly contribute to the glycolytic pathway by providing carbon to pyruvate and, subsequently, lactate. Thus, the flux rate model of lactate production/consumption rate was updated as:

$$v_3 = v_{\max,3f} \times \frac{EGLC}{K_{m,EGLC} \times \left(1 + \frac{K_{a,EGLN}}{EGLN}\right) + EGLC} - v_{\max,3r} \times \frac{ELAC}{K_{m,ELAC} + ELAC}.$$

R3

In accordance with Provost et al. (2006) [42], for simplicity, only two phase transitions were considered: from exponential growth phase ($z = 0$) to stationary phase ($z = 1$), and from stationary phase ($z = 1$) to decline phase ($z = 2$), with other transitions assumed to have negligible probabilities.

4.2 Cell Culture Process Prediction and Prediction Uncertainty Quantification

The predictive efficacy of the proposed multi-scale mechanistic model was evaluated using the dataset $\mathcal{D} = \{\mathbf{s}_{[t_0:t_H]}^{(b)}\}_{b=1}^B$, which consists of $B = 6$ fed-batch cultures. To simulate dynamic cell culture data collection and assess the model’s capability for rolling forecasts, the **(1) ℓ -steps look-ahead forward prediction** performance was studied. At each current time t_h for the b -th batch, the model was trained on a dataset comprising measurements collected up to t_h from the b -th batch, $\mathbf{s}_{[t_0:t_h]}^{(b)}$, along with measurements from all other batches, $\mathbf{s}_{[t_0:t_H]}^{(-b)}$, which excludes the b -th batch. This predictive analytics can support robust control guiding strategic decision making for end-to-end culture processes. Additionally, the **(2) Extrapolation whole-trajectory prediction** was performed. For each b -th batch, the model was trained using the remaining dataset $\mathbf{s}_{[t_0:t_H]}^{(-b)}$. The entire trajectory for the b -th batch was then predicted using only the initial state measurement, $\mathbf{s}_0^{(b)}$. This approach enables the model to support the optimal design of experiments (DoE) through *in silico* simulations. In **(3) Prediction of metabolic flux**, the dynamics of critical metabolic fluxes were predicted throughout the process, providing detailed insights into key metabolic mechanisms.

(1) ℓ -steps look-ahead forward prediction

In this study, the sampling interval for offline measurements was 1 day; accordingly, prediction intervals of 1-day, 3-day, and 5-day were recorded. The WAPE, calculated using Equation (10) for these look-ahead predictions, is summarized in Table 1, demonstrating the model’s promising accuracy across varying prediction horizons.

Table 1: WAPE for 1-Day, 3-Day, and 5-Day Look-Ahead Predictions

		1-Day Prediction	3-Day Prediction	5-Day Prediction
Case A	Rep1	7.8%	8.5%	9.1%
	Rep2	8.3%	8.6%	9.2%
	Rep3	7.3%	8.6%	9.2%
Case B	Rep1	6.5%	8.1%	8.4%
	Rep2	7.6%	8.5%	8.6%
	Rep3	6.1%	7.7%	8.4%

The coverage of the 95% and 90% PIs, accounting for the inherent stochasticity of cell culture processes and batch-to-batch variations, was calculated for 1-day, 3-day, and 5-day look-ahead forward predictions using Equation (11). The results, summarized in Table 2, demonstrate the multi-scale mechanistic model’s ability to accurately predict the dynamics and interdependencies of multivariate cell culture process metabolism. The PIs effectively capture batch-to-batch variations and stochastic behavior, with coverage closely aligning with nominal values even for longer look-ahead horizons, such as 3 and 5 days.

Table 2: Coverage of PIs for 1-Day, 3-Day, and 5-Day Look-Ahead Predictions

		1-Day Prediction		3-Day Prediction		5-Day Prediction	
		95% PI	90% PI	95% PI	90% PI	95% PI	90% PI
Case A	Rep1	93.4%	89.0%	92.6%	88.5%	92.2%	87.4%
	Rep2	92.8%	88.5%	92.3%	87.8%	91.5%	87.7%
	Rep3	92.2%	91.7%	92.2%	87.9%	92.1%	87.0%
Case B	Rep1	94.2%	91.2%	93.3%	88.5%	93.1%	88.0%
	Rep2	93.8%	89.2%	92.2%	88.9%	92.4%	88.6%
	Rep3	94.1%	92.1%	93.8%	89.0%	93.1%	88.0%

Overall, the proposed multi-scale mechanistic model demonstrates robust predictive capabilities, even as the prediction horizon increases. This robustness is primarily attributed to the model’s foundation in single-cell mechanisms, encompassing metabolic dynamics and phase transitions, which enable effective data integration and accurate interpretable long-term predictions. Such performance is challenging to achieve with purely data-driven time series models that tend to fit the patterns without exploring the foundation mechanisms. Consequently, the proposed model provides a reliable support for developing optimal and robust control strategies for end-to-end cell culture processes.

(2) Extrapolation whole-trajectory prediction

The model’s extrapolation predictions for Case A Rep 1 were assessed using the multi-scale mechanistic model trained on the remaining datasets, as shown in Figure 5. The predictions for viable cell density and key metabolites—including glucose, lactate, IgG, glutamine, glutamate, leucine, isoleucine, and valine—demonstrated strong agreement with experimental measurements. Specifically, (1) the point estimates, derived from the prediction mean, closely matched the measured values, and (2) the multivariate cell culture trajectory observations fell within the prediction intervals. Extrapolation whole-trajectory predictions for other batches are presented in Figures A.2 to A.3 in Appendix E.

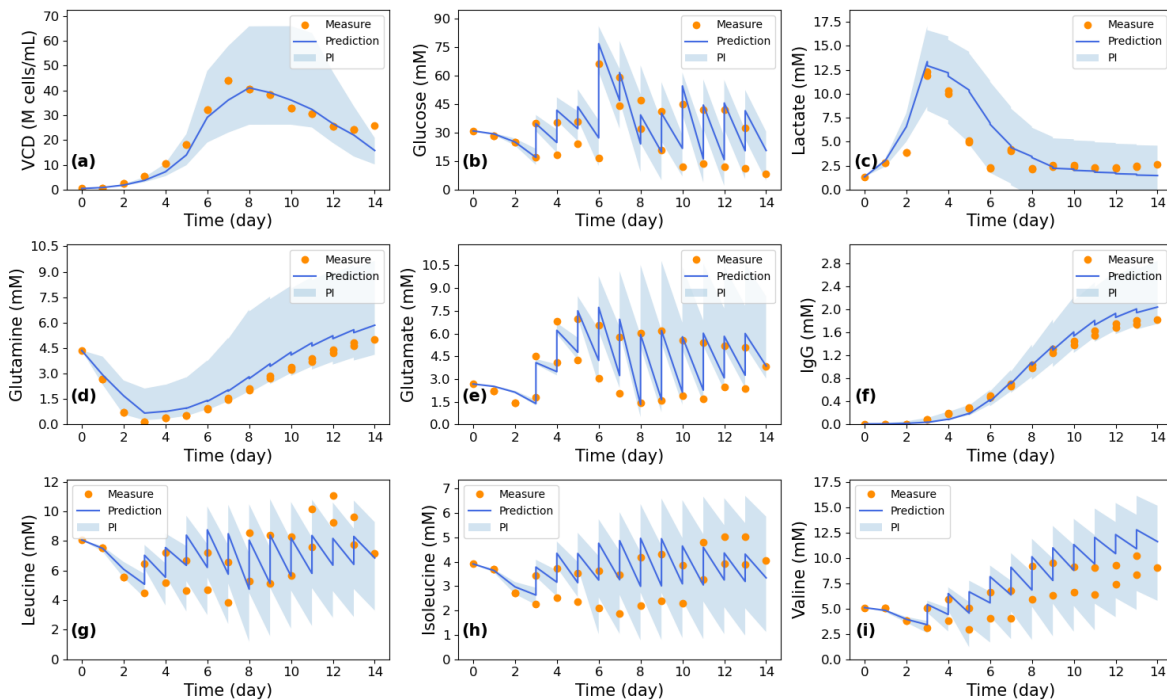


Figure 5: Cell characteristics prediction for Case A Rep1, utilizing a dynamic model trained on the alternative datasets, include: (a) VCD; (b) glucose; (c) lactate; (d) IgG (titer); (e) glutamine; (f) glutamate; (g) leucine; (h) isoleucine; and (i) valine. Actual measurements are denoted by orange dots, and the blue area signifies the 95% prediction interval.

(3) Prediction of metabolic flux

The predictions of metabolic flux dynamics for CHO cell culture are shown in Figure 6. For a more concise and structured presentation of the results, the flux dynamics are categorized by distinct culture phases: early exponential growth phase (day 0 to day 3), late exponential growth phase (day 4 to day 6), stationary phase (day 7 to day 9), and decline phase (day 9 onwards). The similar glucose consumption rates between Case A and Case B ($p > 0.05$), as depicted in Figure 6(b), indicate that both cases exhibited parallel metabolic demands and glycolytic efficiency when nutrients are plentiful. This observation suggests that the foundational metabolic pathways are similarly active in both cases, indicating a uniform metabolic response to nutrient availability at this stage. Figure 3(d) shows that Case B started with a significantly higher glutamine concentration than Case A ($p \leq 0.05$), resulting in a markedly increased glutamine consumption rate for the cells during early exponential phase ($p \leq 0.05$), as shown in Figure 6(d). The significantly higher lactate production rate in Case B ($p \leq 0.05$), along with a lower glutamate consumption rate compared to Case A ($p \leq 0.05$), as shown in Figures 6(c) and (e), could be attributed to metabolic feedback control in response to elevated glutamine consumption for cells during early exponential phase. The increased glutamine availability in Case B enhances glycolysis, leading to higher lactate production, while reduced glutamate consumption suggests that CHO cells are utilizing glutamine more directly, bypassing the need for extensive glutamate conversion. This metabolic adjustment demonstrates how cells dynamically regulate the internal fluxes to optimize growth and productivity based on nutrient availability.

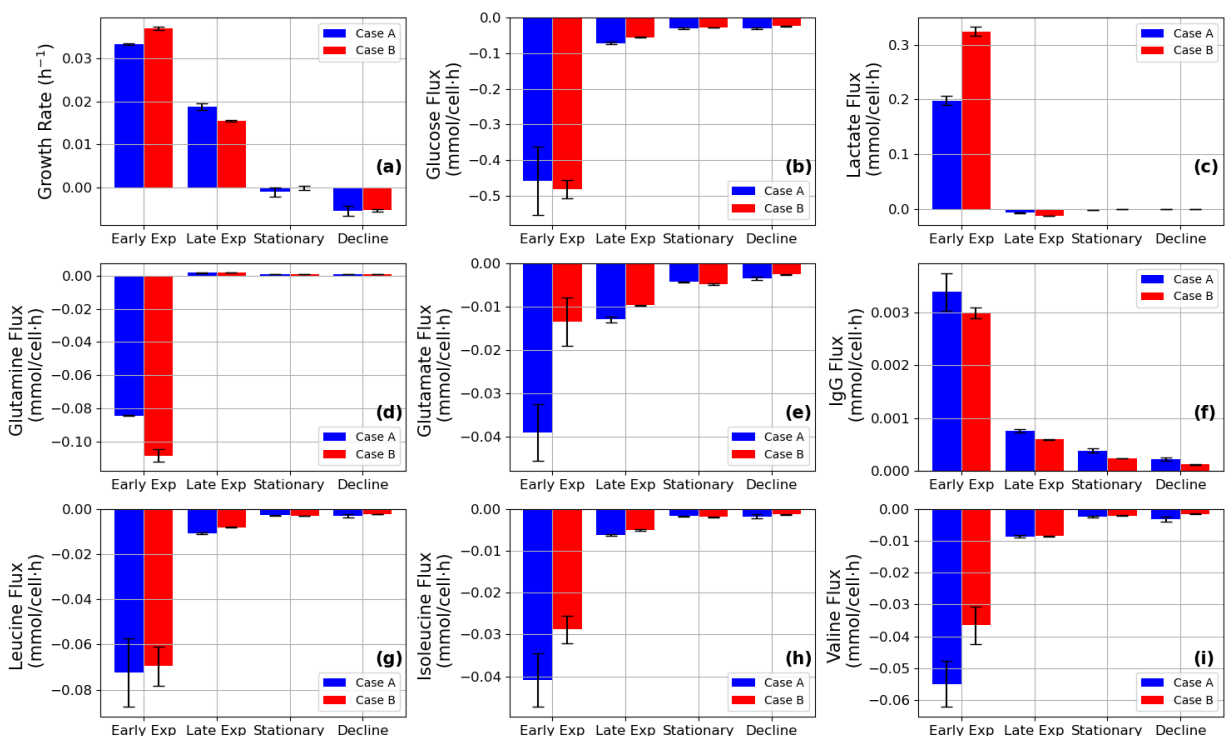


Figure 6: Growth rate and metabolite uptake/secretion flux profiles for CHO VRC01 cell cultures. Illustrated parameters include: (a) VCD; (b) glucose; (c) lactate; (d) IgG (titer); (e) glutamine; (f) glutamate; (g) leucine; (h) isoleucine; and (i) valine. Cultures in Case A are depicted in blue, whereas those in Case B are shown in red. The bars represent the prediction mean, with error bars indicating the prediction standard deviation.

Figure 6(f) illustrates a consistent decline in the synthesis rate of recombinant protein titers throughout the cell culture and biomanufacturing process. This reduction in protein productivity has been extensively discussed and attributed to genomic instability, as reported by Chitwood et al. (2023) [6]. Furthermore, long-term cultured cells, affected by the genomic instability, show altered carbon metabolism, results in decreased protein productivity [8, 5]. Another potential reason could be elevated levels of reactive oxygen species (ROS) during the culture, which trigger oxidative stress responses and reallocate energy away from protein production. Prolonged accumulation of ROS can cause irreversible damage to cellular components, ultimately compromising cell health and viability [44, 20].

After straightforward calculations, it was observed that, under the control experimental setting, there was a gradual decrease in TCA cycle flux rates as the cultures approached the end, consistent with findings reported in a previous

study [1]. The dynamic profiles of the remaining metabolite fluxes of interest (i.e., ammonia, alanine, aspartate, and serine) were presented in the right column of Figure A.1 in Appendix D.

5 Conclusions

This study proposed a comprehensive multi-scale mechanistic model with a bottom-up and top-down structure that captures the time-varying dynamics and regulatory mechanisms of CHO cell cultures by integrating interactions across molecular, cellular, and macroscopic scales. The model effectively describes the metabolic phase shifts observed in CHO cell cultures, with a focus on key metabolic pathways, including glycolysis, the TCA cycle, the PPP, and amino acid metabolism. This multi-scale model has a modular design that integrates three critical modules or components spanning cellular- to macro-kinetics: (1) a stochastic mechanistic model for single-cell metabolic reaction networks; (2) a probabilistic model for single-cell metabolic phase transitions; and (3) a macro-kinetics model for heterogeneous cell populations encompassing cells in various metabolic phases. These modules collectively address the primary factors driving process dynamics and variability in cell cultures, rooted in cellular metabolism.

By integrating heterogeneous online and offline measures, such as viable cell density, metabolite concentrations, dissolved oxygen, and other bioreactor conditions, this multi-scale model provides a robust framework to advance the understanding of cell responses to feeding strategies, oxygen control, and environmental perturbations. Calibrated using time-course measurements, the model accurately predicts the multivariate output trajectory, including cell growth, recombinant proteins production, and state transitions under varying culture conditions. This capability enables reliable predictions and quantifies prediction uncertainty in metabolic profiles and cell population dynamics, addressing critical gaps in existing models. Furthermore, this model with a modular design can facilitate flexible *in silico* simulations. The proposed framework establishes a strong foundation for the development of bioprocessing models and predictive analysis, leveraging mechanistic insights to support end-to-end cell culture optimization and strategic control strategies. Although developed for CHO cells, this modeling framework is general and adaptable to other mammalian cell systems, offering valuable insights for advanced biomanufacturing and process analytical technology applications.

Acknowledge

The authors acknowledge the funding support from the National Institute of Standards and Technology (Grants 70NANB17H002 and 70NANB21H086) to Dr. Wei Xie and the National Science Foundation (Grant OIA-1736123 and EEC-2100442) to Dr. Sarah W. Harcum. Drs. Xie and Harcum are the co-corresponding authors.

Authorship

Keqi Wang: Conceptualization, Formal analysis, Investigation, Methodology, Software, Visualization, and Writing – original draft. **Sarah W. Harcum:** Data curation, Funding acquisition, Methodology, Visualization, Supervision, and Writing – review & editing. **Wei Xie:** Conceptualization, Funding acquisition, Methodology, Project administration, Resources, Supervision, and Writing – review & editing.

References

- [1] Woo Suk Ahn and Maciek R Antoniewicz. Metabolic flux analysis of cho cells at growth and non-growth phases using isotopic tracers and mass spectrometry. *Metabolic engineering*, 13(5):598–609, 2011.
- [2] Maciek R. Antoniewicz. Methods and advances in metabolic flux analysis: a mini-review. *Journal of Industrial Microbiology & Biotechnology*, 42(3):317–325, 2015.
- [3] Maciek R Antoniewicz. A guide to ¹³C metabolic flux analysis for the cancer biologist. *Experimental & molecular medicine*, 50(4):1–13, 2018.
- [4] Paige K Arnold and Lydia WS Finley. Regulation and function of the mammalian tricarboxylic acid cycle. *Journal of Biological Chemistry*, 299(2), 2023.
- [5] Laura A Bailey, Diane Hatton, Ray Field, and Alan J Dickson. Determination of chinese hamster ovary cell line stability and recombinant antibody expression during long-term culture. *Biotechnology and bioengineering*, 109(8):2093–2103, 2012.
- [6] Dylan G Chitwood, Qinghua Wang, Stephanie R Klaubert, Kiana Green, Cathy H Wu, Sarah W Harcum, and Christopher A Sasaki. Microevolutionary dynamics of eccdna in chinese hamster ovary cells grown in fed-batch cultures under control and lactate-stressed conditions. *Scientific Reports*, 13(1):1200, 2023.

- [7] Kevin M Christmas and James B Bassingthwaighe. Equations for o₂ and co₂ solubilities in saline and plasma: combining temperature and density dependences. *Journal of applied physiology*, 122(5):1313–1320, 2017.
- [8] Janet Chusainow, Yuan Sheng Yang, Jessna HM Yeo, Poh Choo Toh, Parisa Asvadi, Niki SC Wong, and Miranda GS Yap. A study of monoclonal antibody-producing cho cell lines: What makes a stable high producer? *Biotechnology and bioengineering*, 102(4):1182–1196, 2009.
- [9] Tiago Costa Leite, Daniel Da Silva, Raquel Guimarães Coelho, Patricia Zancan, and Mauro Sola-Penna. Lactate favours the dissociation of skeletal muscle 6-phosphofructo-1-kinase tetramers down-regulating the enzyme and muscle glycolysis. *Biochemical Journal*, 408(1):123–130, 2007.
- [10] Scott B Crown, Nicholas Marze, and Maciek R Antoniewicz. Catabolism of branched chain amino acids contributes significantly to synthesis of odd-chain and even-chain fatty acids in 3t3-l1 adipocytes. *PLoS one*, 10(12):e0145850, 2015.
- [11] Wentao Dong, Sun Jin Moon, Joanne K Kelleher, and Gregory Stephanopoulos. Dissecting mammalian cell metabolism through ¹³c-and ²h-isotope tracing: interpretations at the molecular and systems levels. *Industrial & Engineering Chemistry Research*, 59(6):2593–2610, 2019.
- [12] Ralf Dressel. Effects of histocompatibility and host immune responses on the tumorigenicity of pluripotent stem cells. In *Seminars in immunopathology*, volume 33, page 573. Springer, 2011.
- [13] Felix Garcia-Ochoa and Emilio Gomez. Bioreactor scale-up and oxygen transfer rate in microbial processes: an overview. *Biotechnology advances*, 27(2):153–176, 2009.
- [14] Atefeh Ghorbaniaghdam, Jingkui Chen, Olivier Henry, and Mario Jolicoeur. Analyzing clonal variation of monoclonal antibody-producing CHO cell lines using an *in silico* metabolomic platform. *PLoS one*, 9(3):e90832, 2014.
- [15] Atefeh Ghorbaniaghdam, Olivier Henry, and Mario Jolicoeur. A kinetic-metabolic model based on cell energetic state: study of CHO cell behavior under Na-butyrate stimulation. *Bioprocess and biosystems engineering*, 36:469–487, 2013.
- [16] Atefeh Ghorbaniaghdam, Olivier Henry, and Mario Jolicoeur. An *in-silico* study of the regulation of CHO cells glycolysis. *Journal of theoretical biology*, 357:112–122, 2014.
- [17] Daniel T Gillespie. Exact stochastic simulation of coupled chemical reactions. *The journal of physical chemistry*, 81(25):2340–2361, 1977.
- [18] Daniel T Gillespie. The chemical langevin equation. *The Journal of Chemical Physics*, 113(1):297–306, 2000.
- [19] MW Glacken, E Adema, and AJ Sinskey. Mathematical descriptions of hybridoma culture kinetics: I. Initial metabolic rates. *Biotechnology and bioengineering*, 32(4):491–506, 1988.
- [20] Michael W Handlogten, Min Zhu, and Sanjeev Ahuja. Intracellular response of cho cells to oxidative stress and its influence on metabolism and antibody production. *Biochemical Engineering Journal*, 133:12–20, 2018.
- [21] Sarah W Harcum, Kathryn S Elliott, Bradley A Skelton, Stephanie R Klaubert, Hussain Dahodwala, and Kelvin H Lee. Pid controls: The forgotten bioprocess parameters. *Discover Chemical Engineering*, 2(1):1, 2022.
- [22] Cameron Harrington, Michaela Jacobs, Quentin Bethune, Taylor Kalomeris, Gregory W Hiller, and Bhanu Chandra Mulukutla. Production of butyrate and branched-chain amino acid catabolic byproducts by cho cells in fed-batch culture enhances their specific productivity. *Biotechnology and Bioengineering*, 118(12):4786–4799, 2021.
- [23] T Hassell, S Gleave, and M Butler. Growth inhibition in animal cell culture: The effect of lactate and ammonia. *Applied biochemistry and biotechnology*, 30:29–41, 1991.
- [24] Milan Holeček. Branched-chain amino acids in health and disease: metabolism, alterations in blood plasma, and as supplements. *Nutrition & metabolism*, 15(1):1–12, 2018.
- [25] HS Hundal, MJ Rennie, and PW Watt. Characteristics of acidic, basic and neutral amino acid transport in the perfused rat hindlimb. *The Journal of physiology*, 408(1):93–114, 1989.
- [26] Marija Ivarsson, Heeju Noh, Massimo Morbidelli, and Miroslav Soos. Insights into pH-induced metabolic switch by flux balance analysis. *Biotechnology Progress*, 31(2):347–357, 2015.
- [27] Matthew D Johnston, Carina M Edwards, Walter F Bodmer, Philip K Maini, and S Jonathan Chapman. Mathematical modeling of cell population dynamics in the colonic crypt and in colorectal cancer. *Proceedings of the National Academy of Sciences*, 104(10):4008–4013, 2007.
- [28] Daniel J Kiviet, Philippe Nghe, Noreen Walker, Sarah Boulineau, Vanda Sunderlikova, and Sander J Tans. Stochasticity of metabolism and growth at the single-cell level. *Nature*, 514(7522):376–379, 2014.

- [29] Sarantos Kyriakopoulos, Kok Siong Ang, Meiyappan Lakshmanan, Zhuangrong Huang, Seongkyu Yoon, Rudiyanto Gunawan, and Dong-Yup Lee. Kinetic modeling of mammalian cell culture bioprocessing: The quest to advance biomanufacturing. *Biotechnology Journal*, 13(3):1700229, 2018.
- [30] Robert W Leighty and Maciek R Antoniewicz. Dynamic metabolic flux analysis (DMFA): a framework for determining fluxes at metabolic non-steady state. *Metabolic engineering*, 13(6):745–755, 2011.
- [31] Ningning Ma, JoAnn Ellet, Centy Okediadi, Paul Hermes, Ellen McCormick, and Susan Casnocha. A single nutrient feed supports both chemically defined ns0 and cho fed-batch processes: Improved productivity and lactate metabolism. *Biotechnology progress*, 25(5):1353–1363, 2009.
- [32] Gagandeep Mann, Stephen Mora, Glory Madu, and Olasunkanmi AJ Adegoke. Branched-chain amino acids: catabolism in skeletal muscle and implications for muscle and whole-body metabolism. *Frontiers in Physiology*, 12:702826, 2021.
- [33] I Martínez-Monge, R Roman, P Comas, A Fontova, M Lecina, A Casablancas, and JJ Cairó. New developments in online our monitoring and its application to animal cell cultures. *Applied microbiology and biotechnology*, 103:6903–6917, 2019.
- [34] Warren L McCabe, Julian C Smith, and Peter Harriott. *Unit operations of chemical engineering*. McGraw-hill, 1993.
- [35] Bhanu Chandra Mulukutla, Michael Gramer, and Wei-Shou Hu. On metabolic shift to lactate consumption in fed-batch culture of mammalian cells. *Metabolic engineering*, 14(2):138–149, 2012.
- [36] Bhanu Chandra Mulukutla, Andrew Yongky, Simon Grimm, Prodromos Daoutidis, and Wei-Shou Hu. Multiplicity of steady states in glycolysis and shift of metabolic state in cultured mammalian cells. *PLoS One*, 10(3):e0121561, 2015.
- [37] K Sreekumaran Nair and Kevin R Short. Hormonal and signaling role of branched-chain amino acids. *The Journal of nutrition*, 135(6):1547S–1552S, 2005.
- [38] Jens Niklas and Elmar Heinzle. Metabolic flux analysis in systems biology of mammalian cells. *Genomics and Systems Biology of Mammalian Cell Culture*, pages 109–132, 2012.
- [39] Ryan P Nolan and Kyongbum Lee. Dynamic model of CHO cell metabolism. *Metabolic engineering*, 13(1):108–124, 2011.
- [40] Conor M O’Brien, Qi Zhang, Prodromos Daoutidis, and Wei-Shou Hu. A hybrid mechanistic-empirical model for in silico mammalian cell bioprocess simulation. *Metabolic Engineering*, 66:31–40, 2021.
- [41] Magdalena Pappenreiter, Bernhard Sissolak, Wolfgang Sommeregger, and Gerald Striedner. Oxygen uptake rate soft-sensing via dynamic k l a computation: Cell volume and metabolic transition prediction in mammalian bioprocesses. *Frontiers in Bioengineering and Biotechnology*, 7:195, 2019.
- [42] Agnès Provost, G Bastin, SN Agathos, and Y J Schneider. Metabolic design of macroscopic bioreaction models: application to chinese hamster ovary cells. *Bioprocess and biosystems engineering*, 29:349–366, 2006.
- [43] Lake-Ee Quek, Stefanie Dietmair, Jens O Krömer, and Lars K Nielsen. Metabolic flux analysis in mammalian cell culture. *Metabolic engineering*, 12(2):161–171, 2010.
- [44] Anu Rahal, Amit Kumar, Vivek Singh, Brijesh Yadav, Ruchi Tiwari, Sandip Chakraborty, and Kuldeep Dhama. Oxidative stress, prooxidants, and antioxidants: the interplay. *BioMed research international*, 2014(1):761264, 2014.
- [45] Araceli Rivera-Ordaz, Valeria Peli, Paolo Manzini, Mario Barilani, and Lorenza Lazzari. Critical Analysis of cGMP Large-Scale Expansion Process in Bioreactors of Human Induced Pluripotent Stem Cells in the Framework of Quality by Design. *BioDrugs*, 35(6):693–714, 2021.
- [46] Claudia Salcedo, Jens V Andersen, Kasper Tore Vinten, Lars H Pinborg, Helle S Waagepetersen, Kristine K Freude, and Blanca I Aldana. Functional metabolic mapping reveals highly active branched-chain amino acid metabolism in human astrocytes, which is impaired in ipsc-derived astrocytes in alzheimer’s disease. *Frontiers in aging neuroscience*, 13:736580, 2021.
- [47] David Schnoerr, Guido Sanguinetti, and Ramon Grima. Approximation and inference methods for stochastic biochemical kinetics—a tutorial review. *Journal of Physics A: Mathematical and Theoretical*, 50(9):093001, 2017.
- [48] Neelanjan Sengupta, Steven T Rose, and John A Morgan. Metabolic flux analysis of CHO cell metabolism in the late non-growth phase. *Biotechnology and bioengineering*, 108(1):82–92, 2011.

- [49] Benjamin F Synoground, Claire E McGraw, Kathryn S Elliott, Christina Leuze, Jada R Roth, Sarah W Harcum, and Nicholas R Sandoval. Transient ammonia stress on chinese hamster ovary (cho) cells yield alterations to alanine metabolism and igg glycosylation profiles. *Biotechnology Journal*, 16(7):2100098, 2021.
- [50] Diana Szélieová, David E Ruckerbauer, Sarah N Galleguillos, Lars B Petersen, Klaus Natter, Michael Hanscho, Christina Troyer, Tim Causon, Harald Schoeny, Hanne B Christensen, et al. What cho is made of: Variations in the biomass composition of chinese hamster ovary cell lines. *Metabolic engineering*, 61:288–300, 2020.
- [51] Neil Templeton, Jason Dean, Pranhitha Reddy, and Jamey D Young. Peak antibody production is associated with increased oxidative metabolism in an industrially relevant fed-batch cho cell culture. *Biotechnology and bioengineering*, 110(7):2013–2024, 2013.
- [52] Mona K Tonn, Philipp Thomas, Mauricio Barahona, and Diego A Oyarzún. Stochastic modelling reveals mechanisms of metabolic heterogeneity. *Communications biology*, 2(1):108, 2019.
- [53] Marshall Trout, Sarah W Harcum, and Richard E Groff. Sensitive real-time on-line estimator for oxygen transfer rates in fermenters. *Journal of Biotechnology*, 358:92–101, 2022.
- [54] USGS. U.s. geological survey, 2011. 2022.
- [55] Klaas Van't Riet. Review of measuring methods and results in nonviscous gas-liquid mass transfer in stirred vessels. *Industrial & Engineering Chemistry Process Design and Development*, 18(3):357–364, 1979.
- [56] Gary Walsh and Eithne Walsh. Biopharmaceutical benchmarks 2022. *Nature Biotechnology*, 40(12):1722–1760, 2022.
- [57] Keqi Wang, Wei Xie, and Sarah W Harcum. Metabolic regulatory network kinetic modeling with multiple isotopic tracers for ipscs. *Biotechnology and Bioengineering*, 121(4):1335–1353, 2024.
- [58] Wolfgang Wiechert, Michael Möllney, Sören Petersen, and Albert A De Graaf. A universal framework for ^{13}C metabolic flux analysis. *Metabolic engineering*, 3(3):265–283, 2001.
- [59] Ping Xu, Colleen Clark, Todd Ryder, Colleen Sparks, Jiping Zhou, Michelle Wang, Reb Russell, and Charo Scott. Characterization of tap ambr 250 disposable bioreactors, as a reliable scale-down model for biologics process development. *Biotechnology progress*, 33(2):478–489, 2017.
- [60] Jamey D Young. Metabolic flux rewiring in mammalian cell cultures. *Current opinion in biotechnology*, 24(6):1108–1115, 2013.

A Appendix: Oxygen Transfer Rate Calculation

The Stationary Liquid Mass Balance (SLMB) method [33, 41, 53] was used to obtain the OTR referenced in the Section 2.2 . Specifically, OTR is defined by Equation (12):

$$OTR = k_L a (C^* - C_L), \quad (12)$$

where $k_L a$ is the volumetric mass transfer coefficient (h^{-1}) and C^* represents liquid oxygen saturation constant (mg/L). Henry's law [53] is used to account for oxygen enrichment at inlet gas reported as y_0 (mol%). DO is used to estimate both C_L and C^* as shown in Equations (13) and (14):

$$C_L = C_{cal}^* \frac{DO}{100}, \quad (13)$$

$$C^* = C_{cal}^* \frac{y_0}{y_{0,cal}}, \quad (14)$$

where $y_{0,cal}$ represents the inlet oxygen concentration (mol%), and C_{cal}^* represents liquid oxygen saturation constant (mg/L) for the media without cell with 95% air and 5% CO_2 gas flow rate ratios.

The $k_L a$ value was estimated from the Van't Riet's study [55] given in Equation (15):

$$k_L a = K \left(\frac{P_g}{V} \right)^a (v_s)^b, \quad (15)$$

where P_g represents the gassed power (W), V is the liquid volume (L), v_s is the superficial gas velocity (m/s), and K , a , b are empirical constants for the specific vessel configuration. To determine the gassed power P_g , the ungassed power (P_0) is estimated from the definition of the Power Number given by Equation (16),

$$P_0 = N_p \rho d^5 n^3, \quad (16)$$

where N_p is the Power Number (unitless), ρ is the liquid density (kg/m^3), d is the impeller diameter (m), and n is the stir speed (rps). The N_p is a function of the Reynolds number (Re). For ambr250 with marine impeller, the stir speed ranges from 50 to 660 rps; therefore, N_p was considered a constant value [34].

The relationship between P_g and P_0 can vary across different systems. In ambr250, the Aeration number (N_{Ae}) ranges from 0.001 to 0.009 (unitless), and the superficial gas velocity v_s ranges from 2×10^{-5} to 1×10^{-4} m/s. This results in a proportional relationship between P_g and P_0 given by $P_g = c_1 P_0$, where c_1 is a constant for these limited operation conditions and $c_1 < 1$ since $P_g < P_0$ always [13].

By substituting Equation (16) into Equation (15) and applying a logarithmic transformation, $k_L a$ is given in Equation (17):

$$\ln(k_L a) = \ln(K) + a \ln \left(\frac{c_1 N_p \rho d^5}{V} n^3 \right) + b \ln(v_s). \quad (17)$$

Since the superficial gas velocity (v_s) is proportional to the ratio of the total gas mass flow rate to the liquid volume denoted by $\frac{M_f}{V}$, v_s can be represented as $v_s = c_2 \frac{M_f}{V}$. Thus, Equation (17) for $k_L a$ after substitution results in Equation (18):

$$\begin{aligned} \ln(k_L a) &= \ln(K) + a \ln \left(\frac{c_1 N_p \rho d^5}{V} \right) + a \ln(n^3) + b \ln \left(\frac{M_f}{V} \right) + b \ln(c_2) \\ &= \ln(K^*) + a \ln(n^3) + b \ln \left(\frac{M_f}{V} \right), \end{aligned} \quad (18)$$

where $K^* = K \left(\frac{c_1 N_p \rho d^5}{V} \right)^a c_2^b$.

Finally, Equations (12)–(14) and (18) are combined:

$$OTR = K^* (n^3)^a \left(\frac{M_f}{V} \right)^b \left(C_{cal}^* \frac{y_0}{y_{0,cal}} - C_{cal}^* \frac{DO}{100} \right). \quad (19)$$

Based on the data provided in Xu et al. (2017) [59], the estimated parameters are $a = 0.48$, $b = 0.54$, and $K^* = 0.0025$ for gas flow rate at 25 mL/min. The liquid oxygen saturation constant and inlet oxygen concentration at calibration are $C_{cal}^* = 6.39$ mg/L for phosphate buffered saline (PBS) [7, 54] and $y_{0,cal} = 20.96\%$ oxygen.

B Appendix: VRC01 Sequence

VRC01 heavy chain: MKWVTFISLLFLFSSAYSEIVLTQSPGTLSPGETAIIISCRTSQYGLAWYQQRPGQAP
RLVIYSGSTRAAGIPDRFSGSRWGPDYNTISNLESGDFGVYYCQQYEFFGQGTKVQVDIKRTVAAPS VFIF
PPSDEQLKSGTASVVCLLNNFYPREAKVQWKVDNALQSGNSQESVTEQDSKDSTYLSSTLTLKADYEKH
KVYACEVTHQGLSSPVTKSFNRGEC

VRC01 heavy chain: MKWVTFISLLFLFSSAYSQVQLVQSGGQMKKPGESMRISCRASGYEFIDCTLNWIRLAP
GKRPEWMGWLKPRGGAVNYARPLQGRVTMTRDVYSDTAFLELRSLTVDDTAVYFCTRGKNC DYNWDFE
HWGRGTPVIVSSASTKGPSVFPLAPSSKSTSGGTAALGCLVKDYFPEPVTVSWNSGALTSGVHTFPAVLQSS
GLYSLSSVTVPSSSLGTQTYICNVNHKPSNTKVDKRVEPKSCDKTHTCPPCPAPELLGGPSVFLFPPKPKDT
LMISRTPEVTCVVVDVSHEDPEVKFNWYVDGVEVHNAKTKPREEQYNSTYRVVSVLTVLHQDWLNGKEY
KCKVSNKALPAPIEKTISKAKGQPREPQVYTLPPSREEMTKNQVSLTCLVKGFYPSDIAVEWESNGQPENNY
KTTTPVLDSDGSFFLYSKLTVDKSRWQQGNV FSCSVMHEALHNHYTQKSLSLSPG

C Appendix: Expectation Maximization Algorithm

The Expectation-Maximization (EM) algorithm is employed to iteratively search for the maximum likelihood estimate (MLE) of the model parameters by addressing the incomplete nature of the observed data. In each i -th iteration, the algorithm operates in two main steps: the Expectation (E) step and the Maximization (M) step.

Expectation (E) Step: To better represent the nonlinear state transitions of cell culture process, each data collection interval of the real observations \mathcal{D} is interpolated by inserting k intermediate state transitions, creating an augmented dataset denoted as \mathcal{D}^* . This synthesized dataset \mathcal{D}^* represents the interpolated data points that fill the gaps between observed measurements, providing a more continuous and comprehensive representation of cell culture process dynamics. In this step, the current parameter estimates $\boldsymbol{\theta}^{(i)}$ are used to estimate the distribution of the missing values conditioned on the observed data \mathcal{D} and the current parameter values: $Q(\boldsymbol{\theta} | \boldsymbol{\theta}^{(i)}) = \mathbb{E}_{\mathcal{D}^* \sim p(\mathcal{D}^* | \mathcal{D}, \boldsymbol{\theta}^{(i)})} [\log P(\mathcal{D}, \mathcal{D}^* | \boldsymbol{\theta})]$, where $Q(\boldsymbol{\theta} | \boldsymbol{\theta}^{(i)})$ is the expected log-likelihood function, and $P(\mathcal{D}, \mathcal{D}^* | \boldsymbol{\theta})$ is the joint likelihood of the observed and interpolated data given the model parameters $\boldsymbol{\theta}$.

Maximization (M) Step: The parameters $\boldsymbol{\theta}$ are updated by maximizing the expected log-likelihood function from the E-step: $\boldsymbol{\theta}^{(i+1)} = \arg \max_{\boldsymbol{\theta}} Q(\boldsymbol{\theta} | \boldsymbol{\theta}^{(i)})$. Both the original dataset \mathcal{D} and the augmented dataset \mathcal{D}^* are used to update the parameter estimates. The combined dataset $\{\mathcal{D}, \mathcal{D}^*\}$ serves as the basis for maximizing the likelihood of the observed and interpolated data, leading to an updated set of parameters $\boldsymbol{\theta}^{(i+1)}$.

Algorithm Implementation: The following steps in Algorithm 1 outline the procedure of the proposed EM algorithm used for parameter estimation for the proposed multi-scale mechanistic model of CHO cell culture process.

Algorithm 1: Expectation-Maximization Algorithm for Model Parameter Estimation

Input: Observed dataset \mathcal{D} , number of subintervals k for each measurement interval, convergence tolerance ξ

Output: Estimated model parameters $\boldsymbol{\theta}$

Initialize: Set initial parameter estimates $\boldsymbol{\theta}^{(0)}$ to plausible starting values and initialize the iteration counter $i = 0$; Divide the original time steps $\{t_h\}_{h=0}^H$, associated with the measurements \mathcal{D} , into a denser set of time steps

$\{t_\eta^*\}_{\eta=0}^{kH}$, where each interval $\Delta t = t_{h+1} - t_h$ is subdivided into k equal subintervals of size $\Delta t^* = \frac{\Delta t}{k}$;

while $\|\boldsymbol{\theta}^{(i+1)} - \boldsymbol{\theta}^{(i)}\| \geq \xi$ **do**

 // E-Step: Interpolation of Missing Data and Synthesis of Augmented Dataset \mathcal{D}^*

 Initialize an empty dataset \mathcal{D}^* for interpolated data points;

for each time step t_η^* in the denser time steps $\{t_\eta^*\}_{\eta=0}^{kH}$ **do**

if data for $\mathbf{X}_{t_\eta^*}$ or $\mathbf{u}_{t_\eta^*}$ are missing **then**

 Interpolate missing values for cell population $\mathbf{X}_{t_\eta^*}$ and extracellular metabolites $\mathbf{u}_{t_\eta^*}$ using previous values $\mathbf{X}_{t_{\eta-1}^*}$ and $\mathbf{u}_{t_{\eta-1}^*}$, along with current parameter estimates $\boldsymbol{\theta}^{(i)}$ via Equations (8) and (9);

 Add the interpolated data points to \mathcal{D}^* ;

end

end

 // M-Step: Parameter Optimization Using the Combined Dataset $\{\mathcal{D}, \mathcal{D}^*\}$

 Update $\boldsymbol{\theta}^{(i+1)}$ by maximizing the log-likelihood function over the combined dataset:

$$\boldsymbol{\theta}^{(i+1)} = \arg \max_{\boldsymbol{\theta}} \sum_{\eta=0}^{kH-1} \log p(\mathbf{X}_{t_{\eta+1}^*}, \mathbf{u}_{t_{\eta+1}^*} | \mathbf{X}_{t_\eta^*}, \mathbf{u}_{t_\eta^*}, \boldsymbol{\theta});$$

 Increment iteration counter: $i = i + 1$;

end

Return: Estimated model parameters $\boldsymbol{\theta}$.

D Appendix: Figure

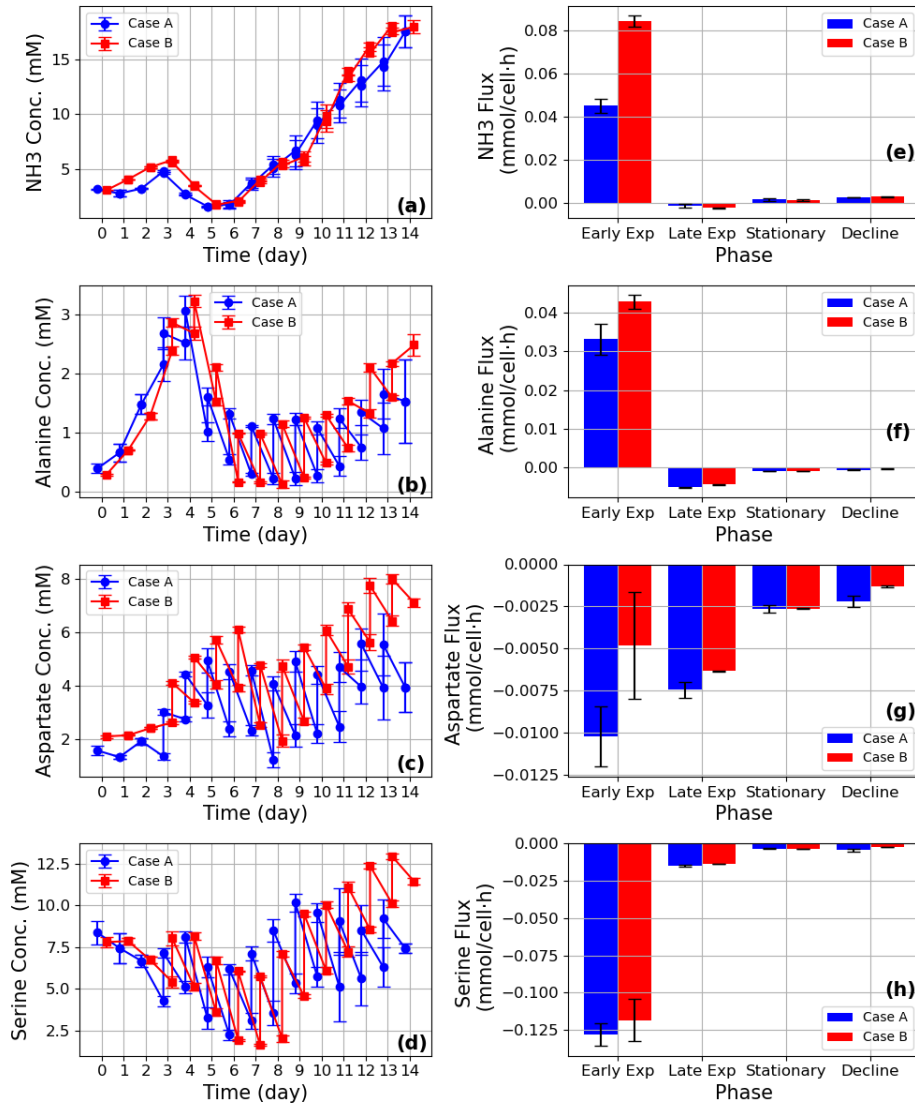


Figure A.1: **Left column:** Growth and cell metabolite profiles for CHO VRC01 cell cultures. Illustrated parameters include: (a) ammonia; (b) alanine; (c) aspartate; (d) serine; Case A cultures are depicted in blue, while Case B cultures are in red. The lines represent the mean values obtained from triplicate cultures, with error bars reflecting the standard deviations. To distinguish overlapping data points, a slight horizontal offset of 0.4 days has been applied between the data points for Case A and Case B. The lines represent the mean values from triplicate cultures, with error bars indicating the standard deviations. **Right column:** Growth Rate and metabolite uptake/secretion flux profiles for CHO VRC01 cell cultures. Illustrated parameters include: (e) ammonia; (f) alanine; (g) aspartate; (h) serine; Cultures in Case A are depicted in blue, whereas those in Case B are shown in red. The bars represent the mean values from triplicate cultures, with error bars indicating the standard deviations.

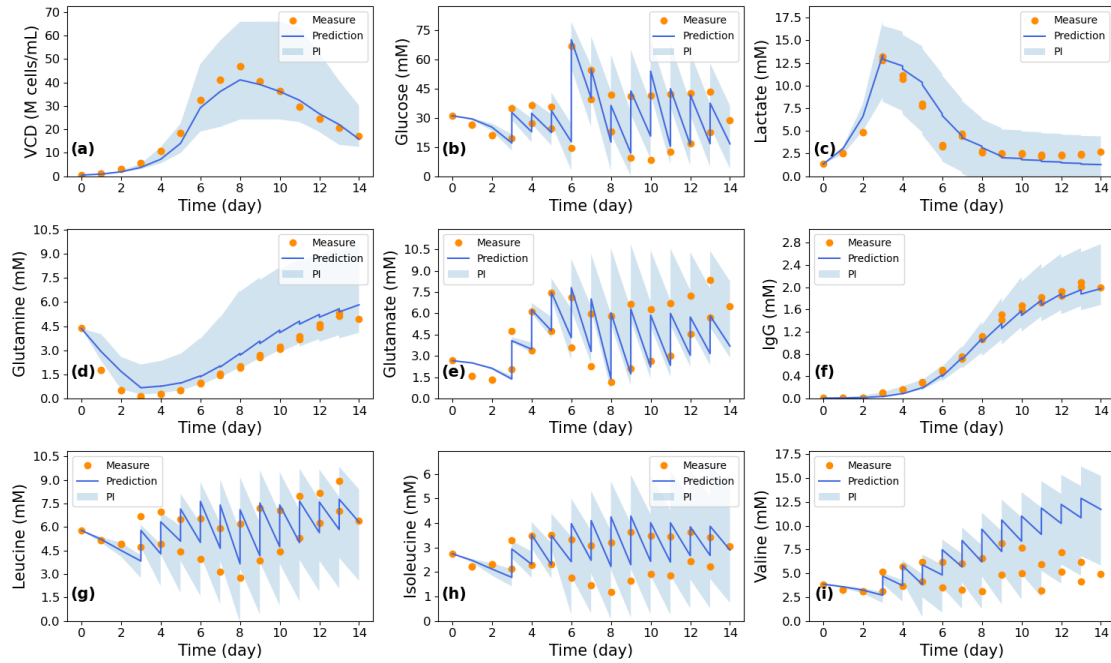


Figure A.2: Cell characteristics prediction for Case A Rep2, utilizing a dynamic model trained on the alternative datasets, include: (a) VCD; (b) glucose; (c) lactate; (d) IgG (titer); (e) glutamine; (f) glutamate; (g) leucine; (h) isoleucine; and (i) valine. Actual measurements are denoted by orange dots, and the blue area signifies the 95% prediction interval.

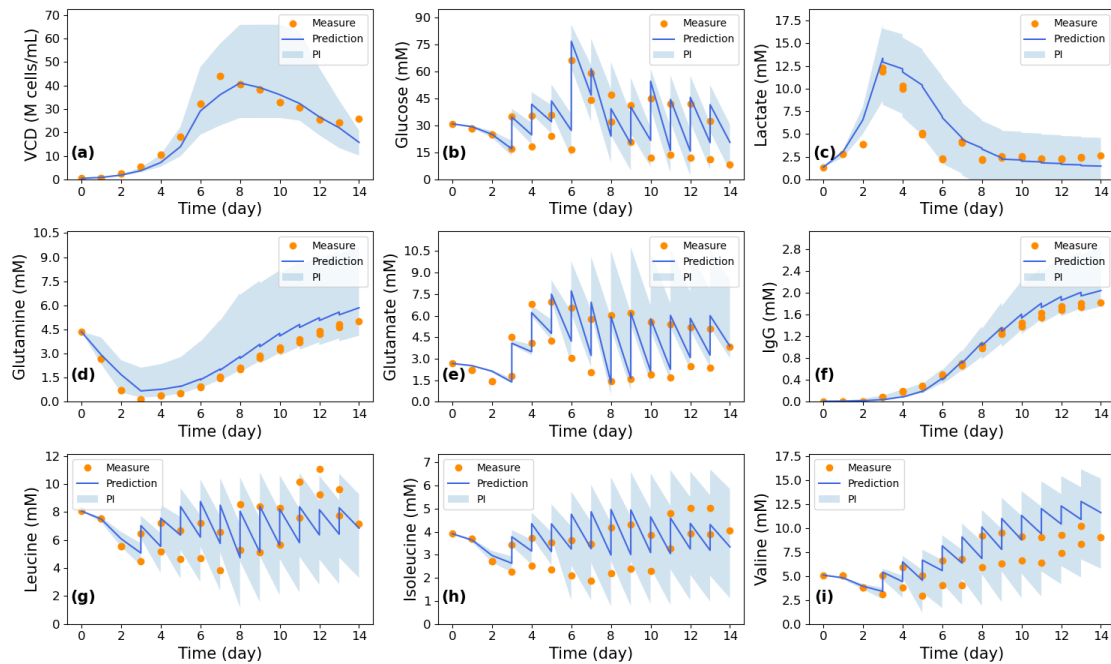


Figure A.3: Cell characteristics prediction for Case B Rep1, utilizing a dynamic model trained on the alternative datasets, include: (a) VCD; (b) glucose; (c) lactate; (d) IgG (titer); (e) glutamine; (f) glutamate; (g) leucine; (h) isoleucine; and (i) valine. Actual measurements are denoted by orange dots, and the blue area signifies the 95% prediction interval.

E Appendix: Table

Table A.1: Reactions for the metabolic network

No.	Pathway
1	EGLC \rightarrow G6P
2	G6P \rightarrow 2 PYR
3	PYR \leftrightarrow LAC
4	LAC \leftrightarrow ELAC
5	GLU + PYR \leftrightarrow AKG + ALA
6	ALA \rightarrow EALA
7	SER \rightarrow PYR + NH ₄
8	ESER \rightarrow SER
9	PYR \rightarrow AcCoA + CO ₂
10	AcCoA + OAA \rightarrow AKG + CO ₂
11	AKG \rightarrow SUC + CO ₂
12	SUC \rightarrow MAL + CO ₂
13	MAL \rightarrow OAA
14	MAL \rightarrow PYR + CO ₂
15	EGLN \rightarrow GLN
16	GLN \leftrightarrow GLU + NH ₄
17	GLU \leftrightarrow AKG + NH ₄
18	GLU \rightarrow EGLU
19	ASP + AKG \leftrightarrow GLU + OAA + NH ₄
20	EASP \rightarrow ASP
21	LEU + AKG \rightarrow GLU + 3 AcCoA
22	ELEU \rightarrow LEU
23	VAL + AKG \rightarrow GLU + SUC + CO ₂
24	EVAL \rightarrow VAL
25	ILE + AKG \rightarrow GLU + SUC + AcCoA
26	EILE \rightarrow ILE
27	66 EALA + 56 EASP + 62 EGLN + 68 EGLU + 166 ESER + 108 ELEU + 38 EILE + 122 EVAL \rightarrow ANTI
28	ANTI \rightarrow EANTI
29	0.39 EALA + 0.26 EASP + 0.32 EGLN + 0.32 EGLU + 0.34 ESER + 0.42 LEU + 0.19 ILE + 0.26 EVAL + 0.11 EGLC \rightarrow BIOM

Table A.2: Biokinetic equations for the metabolites fluxes of the model

No.	Pathway
2	$v_2 = v_{max,2} \times \frac{EGLC}{K_{m,EGLC} + EGLC} \times \frac{K_{i,ELACtoHK}}{K_{i,ELACtoHK} + ELAC} \times \frac{K_{i,ELEUtoHK}}{K_{i,ELEUtoHK} + ELEU}$
3	$v_3 = v_{max,3f} \times \frac{EGLC}{K_{m,EGLC} \times (1 + \frac{K_a,EGLN}{EGLN}) + EGLC} - v_{max,3r} \times \frac{ELAC}{K_{m,ELAC} + ELAC}$
5	$v_5 = v_{max,5f} \times \frac{EGLC}{K_{m,EGLC} + EGLC} - v_{max,5r} \times \frac{EALA}{K_{m,EALA} + EALA}$
7	$v_7 = v_{max,7} \times \frac{ESER}{K_{m,ESER} + ESER}$
16	$v_{16} = v_{max,16f} \times \frac{EGLN}{K_{m,EGLN} + EGLN} \times \frac{K_{i,ELACtoGLNS}}{K_{i,ELACtoGLNS} + ELAC} - v_{max,16r} \times \frac{EGLU}{K_{m,EGLU} + EGLU} \times \frac{NH_4}{K_{m,NH_4} + NH_4}$
17	$v_{17} = v_{max,17f} \times \frac{EGLU}{K_{m,EGLU} + EGLU} - v_{max,17r} \times \frac{NH_4}{K_{m,NH_4} + NH_4}$
19	$v_{19} = v_{max,19f} \times \frac{EASP}{K_{m,EASP} + EASP} - v_{max,19r} \times \frac{EGLU}{K_{m,EGLU} + EGLU} \times \frac{NH_4}{K_{m,NH_4} + NH_4}$
21	$v_{21} = v_{max,21} \times \frac{ELEU}{K_{m,ELEU} + ELEU}$
23	$v_{23} = v_{max,23} \times \frac{EVAL}{K_{m,EVAL} + EVAL}$
25	$v_{25} = v_{max,25} \times \frac{EILE}{K_{m,EILE} + EILE}$
27	$v_{27} = v_{max,27} \times \frac{EGLN}{K_{m,EGLN} + EGLN} \times \frac{EGLU}{K_{m,EGLU} + EGLU} \times \frac{EALA}{K_{m,EALA} + EALA} \times \frac{EASP}{K_{m,EASP} + EASP} \times \frac{ESER}{K_{m,ESER} + ESER} \times \frac{ELEU}{K_{m,ELEU} + ELEU} \times \frac{EILE}{K_{m,EILE} + EILE} \times \frac{EVAL}{K_{m,EVAL} + EVAL}$
29	$v_{29} = v_{max,29} \times \frac{EGLN}{K_{m,EGLN} + EGLN} \times \frac{EGLC}{K_{m,EGLC} + EGLC} \times \frac{EGLU}{K_{m,EGLU} + EGLU} \times \frac{EALA}{K_{m,EALA} + EALA} \times \frac{EASP}{K_{m,EASP} + EASP} \times \frac{ESER}{K_{m,ESER} + ESER} \times \frac{ELEU}{K_{m,ELEU} + ELEU} \times \frac{EILE}{K_{m,EILE} + EILE} \times \frac{EVAL}{K_{m,EVAL} + EVAL}$

Table A.3: Metabolite abbreviations and full names

Abbreviation	Full Name
AcCoA	Acetyl-Coenzyme A
AKG	α -Ketoglutarate
ALA	Alanine
ANTI	Antibody
ASP	Aspartate
BIOM	Biomass
CO2	Carbon dioxide
EALA	Alanine, extracellular
EANTI	Antibody, extracellular
EASP	Aspartate, extracellular
EGLC	Glucose, extracellular
EGLN	Glutamine, extracellular
EGLU	Glutamate, extracellular
EILE	Isoleucine, extracellular
ELAC	Lactate, extracellular
ELEU	Leucine, extracellular
ESER	Serine, extracellular
EVAL	Valine, extracellular
G6P	Glucose-6-phosphate
GLN	Glutamine
GLU	Glutamate
ILE	Isoleucine
LAC	Lactate
LEU	Leucine
MAL	Malate
NH4	Ammonium
OAA	Oxaloacetate
PYR	Pyruvate
SER	Serine
SUC	Succinate
VAL	Valine